

A view of the narrow-line region in the infrared: active galactic nuclei with resolved fine-structure lines in the *Spitzer* archive

K. M. Dasyra^{1,2}, L. C. Ho³, H. Netzer⁴, F. Combes², B. Trakhtenbrot⁴, E. Sturm⁵, L. Armus⁶, D. Elbaz¹

ABSTRACT

We queried the *Spitzer* archive for high-resolution observations with the Infrared Spectrograph of optically selected active galactic nuclei (AGN) for the purpose of identifying sources with resolved fine-structure lines that would enable studies of the narrow-line region (NLR) at mid-infrared wavelengths. By combining 298 *Spitzer* spectra with 6 *Infrared Space Observatory* spectra, we present kinematic information of the NLR for 81 $z \lesssim 0.3$ AGN. We used the [Ne V], [O IV], [Ne III], and [S IV] lines, whose fluxes correlate well with each other, to probe gas photoionized by the AGN. We found that the widths of the lines are, on average, increasing with the ionization potential of the species that emit them. No correlation of the line width with the critical density of the corresponding transition was found. The velocity dispersion of the gas, σ , is systematically higher than that of the stars, σ_* , in the AGN host galaxy, and it scales with the mass of the central black hole, M_{BH} . Further correlations between the line widths and luminosities L , and between L and M_{BH} , are suggestive of a three dimensional plane connecting $\log(M_{\text{BH}})$ to a linear combination of $\log(\sigma)$ and $\log(L)$. Such a plane can be understood within the context of gas motions that are driven by AGN feedback mechanisms, or virialized gas motions with a power-law dependence of the NLR radius on the AGN luminosity. The M_{BH} estimates obtained for 35 type 2 AGN from this plane are consistent with those obtained from the $M_{\text{BH}} - \sigma_*$ relation.

Subject headings: galaxies: active — galaxies: kinematics and dynamics — galaxies: nuclei — galaxies: Seyferts — infrared: galaxies — quasars: emission lines

1. Introduction

Meaningful statistical tests of whether the bulk of black hole (BH) growth precedes, is parallel, or follows the peak of star-formation activity need to rely on the comparison of several observable parameters as a function of look-back time. In addition to the comparison of the star-formation rate (SFR) with the BH accretion rate (e.g., Marconi et al. 2004; Merloni et al. 2004), the comparison of the stellar mass with the BH mass, M_{BH} , that is already accumulated at any given redshift z is also desirable. A significant impediment in performing the latter comparison comes from the fact that rapid BH growth often occurs in highly obscured environments, such as type 2 active galactic nuclei (AGN) and infrared

(IR) bright galaxies. At low z and at low (Seyfert-like) luminosities, L , 50–70% of the AGN are of type 2 (Ho et al. 1997b; Schmitt et al. 2001; Hao et al. 2005). At $z \sim 1$ and at bolometric luminosities that exceed $10^{12} L_{\text{sun}}$, at least 1 out of every 3 AGN is thought to be of type 2 (Lacy et al. 2007; Gilli et al. 2007).

In type 2 systems, the determination of M_{BH} is very challenging. Direct methods of measuring M_{BH} , e.g., by spatially resolved sub-parsec or parsec scale kinematics of stars (Genzel et al. 1997), ionized gas (Harms et al. 1994; Macchetto et al. 1997), or water masers (Miyoshi et al. 1995), can only be applicable to very local objects. An alternative method that is successfully applied to type 1 AGN even at high z (Kaspi et al. 2007) uses the kinematics and the radial extent of gas

clouds that are close enough to the BH to be gravitationally influenced by it. These clouds constitute the AGN broad line region (BLR). Emission lines tracing the BLR, such as $H\beta$, Mg II and C IV, have typical full width at half maxima (FWHM) exceeding 2000 km s^{-1} . The BLR radius is determined by reverberation mapping experiments, which use the natural variability of the AGN continuum and the time-delayed response of the gas (de)excitation to compute the light travel time across the BLR (Blandford & McKee 1982; Peterson 1993; Kaspi et al. 2000). Assuming that the clouds are virialized, their distance from the BH and their velocity dispersion can be used to determine an enclosed dynamical mass and, thus, M_{BH} . However, the method is not applicable to type 2 AGN where the BLR is obscured.

The lines that are seen in both type 1 and type 2 AGN are those that typically originate from gas clouds at a few pc to a few hundreds of pc away from the BH (Netzer 2004; Laor 2007 and references therein). These narrow-line-region (NLR) clouds have FWHM that are typically $\lesssim 1000 \text{ km s}^{-1}$. Using the [O III] 5007 Å line, Nelson & Whittle (1996) demonstrated that the bulk of the gas traced by [O III] has a velocity dispersion that is comparable to that of the stars in the host-galaxy bulge. Subsequently, M_{BH} was found to scale with the width of the [O III] emission (Nelson 2000; Shields et al. 2003; Greene & Ho 2005). A similar result was found for the [N II] line at 6583 Å by Ho (2009).

Optical NLR lines can suffer severe obscuration (Kauffmann et al. 2003). This makes IR wavelengths more reliable and often unique for investigating relations between NLR kinematics and M_{BH} . To optimize the use of narrow lines as gravitational potential tracers for obscured AGN, we performed a similar analysis in mid-infrared (MIR) wavelengths using *Spitzer* and *Infrared Space Observatory* (ISO) high-resolution spectra. We demonstrated that the widths of the NLR lines [Ne V] at $14.32 \mu\text{m}$ and [O IV] at $25.89 \mu\text{m}$ also scale with M_{BH} (Dasyra et al. 2008). This result could provide a means of probing NLR kinematics and weighing BH masses in obscured galaxies at high z with the next generation IR telescopes.

The goal of this paper is to perform an extended study of the NLR kinematics of optically selected type 1 and type 2 AGN in the MIR using all spec-

tra that are available in the *Spitzer* archive. We aim to investigate for differences in the gas kinematics as traced by various fine-structure lines, to test how the gas velocities compare with M_{BH} , and to further estimate the masses of local obscured AGN. For all computations, we use a Λ CDM cosmology with $H_0=70 \text{ km s}^{-1} \text{ Mpc}^{-1}$, $\Omega_m=0.3$, and $\Omega_\Lambda=0.7$.

2. The Sample

To study the NLR gas kinematics as probed by MIR emission lines, we queried the entire *Spitzer* archive for high-resolution observations of AGN obtained with the Infrared Spectrograph (IRS; Houck et al. 2004). These spectra have a resolving power of $\sim 500 \text{ km s}^{-1}$, sufficient for resolving features in the NLR of several local AGN (Dasyra et al. 2008). We downloaded the reserved observations catalog (ROC) after the completion of *Spitzer's* cryogenic mission to ensure that all archival data that can be used for this study are included in our sample. We found 1366 astronomical observation requests (AORs) containing high-resolution IRS spectra of extragalactic sources performed in either single-target or cluster mode.

We matched all IRS targets with optical spectroscopic catalogs of AGN to identify type 1 sources with existing M_{BH} estimates and [O III] 5007 Å detections that are required for the comparison of NLR kinematics at various wavelengths. For this purpose, we used i) the reverberation mapping catalogs of Peterson et al. (2004), Bentz et al. (2006), Bentz et al. (2009), and Denney et al. (2010), ii) the spectroscopic subsample of the Palomar-Green (PG) QSOs (Boroson & Green 1992; Vestergaard & Peterson 2006), iii) the optical spectroscopic catalog of Marziani et al. (2003), iv) the Ho & Kim (2009) catalog of type 1 AGN, v) the Sloan digital sky survey (SDSS) data release 4 AGN catalogs of Kauffmann et al. (2003), of Greene & Ho (2005), and of Netzer & Traktenbrot (2007), and vii) the SDSS data release 7 (DR7). To identify AGN in the DR7, we used the Baldwin et al. (1981) diagnostic diagram of [O III]/ H_β versus [N II]/ H_α with the AGN boundaries as updated by Kewley et al. (2006). We also examined sources that have a QSO target type, or

a broad-line or AGN spectral type subclass assigned by the SDSS pipeline. These samples also include a few type 2 AGN, which we further complemented by matching all IRS targets with the Mulchaey et al. (1994), Turner et al. (1997), Bassani et al. (1999), Zakamska et al. (2003), Reyes et al. (2008), Bennert et al. (2009), and Liu et al. (2009) catalogs. A few additional optical spectra of type 2 AGN were found in Spinelli et al. (2006)

In total, we found and reduced datasets from 370 *Spitzer* AORs, corresponding to high-resolution spectra of 298 sources. Resolved NLR lines were determined from the inspection of the [S IV] $10.51\ \mu\text{m}$, [Ne III] $15.56\ \mu\text{m}$, [O IV] $25.89\ \mu\text{m}$, or [Ne V] $14.32\ \mu\text{m}$ profiles as described in Section 3.2. To these 298 AGN, we added 6 sources with fine structure lines that were similarly resolved by ISO short wavelength spectrograph (SWS) data (Sturm et al. 2002; Dasyra et al. 2008). The redshift distribution of all 304 sources in the final sample is shown in Figure 1. The 42 type 1 AGN and the 39 type 2 AGN that have resolved MIR narrow lines are presented in Tables 1 and 2, respectively.

3. Data Reduction

3.1. Spectral Extraction

We downloaded the *Spitzer* S15.0 pipeline basic calibration data (BCD) files. We used both staring and mapping observations, taken on either single-source or cluster mode.

The BCD files of the long-high (LH) wavelength data of each source were processed by the IDL routine DARK SETTLE, which is posted at the *Spitzer* Science Center (SSC) web site, to correct for gradations of the dark current along the detector that lead to order tilting and mismatch. Using the short-high (SH) BCD files and the dark-settle corrected LH BCD files, we computed the average frame for each set of on-source observations, namely, for each each target, nod position, and module. To identify cosmic ray hits, we also computed the median frame for the same set of observations and compared it to the average frame on a pixel by pixel basis. A pixel was flagged if the difference between the median and the average frame value differed by a factor of more than three times the root-mean square (rms) noise in the me-

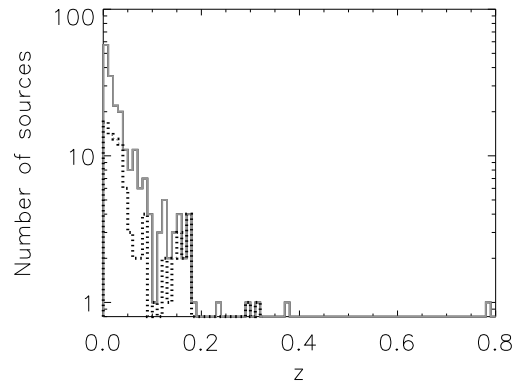


Fig. 1.— Redshift distribution of AGN with MIR [S IV], [Ne III], [O IV], or [Ne V] detections (grey solid line), and redshift distribution of AGN with resolved [S IV], [Ne III], [O IV], or [Ne V] lines (black dotted line).

dian frame. For this pixel, the average value was replaced by the median value. For sources with available observations on sky⁷, we also computed the median sky frame, which we subtracted from the on-source frame.

The next step was the removal of bad and rogue (i.e., slowly varying time response) pixels. We used the individual sky frames to create a generic bad pixel mask for all sources observed in a single *Spitzer* campaign, which we merged with the bad pixel map available at the SSC web site for the same campaign. We then merged this generic mask with the mask of each individual (on-source and on-sky) exposure to create the mask for each science frame, nod position, and module. We proceeded to further masking of outliers, i.e., pixels that were located a couple of columns away from the edges of each spectral order, and that had a value exceeding the rms noise of the science frame. Their values were replaced with the median value of the frame, computed using only pixels in the useful detector range. A final visual inspection and manual cleaning of the science frames was performed using the IRSCLEAN routine. All rogue pixels and outliers were flagged in the mask file.

⁷ Several programs whose scientific goals required only the use of line fluxes (but not the use of equivalent widths or continuum flux measurements) did not acquire sky observations given that the flux of a line does not depend on its underlying continuum level.

The uncertainty of the average on-source frame was calculated as the square root of the sum of the squares of all individual uncertainty files, divided by the number of exposures. When sky observations were available, we computed the sky frame uncertainty in a similar way and combined it with the on-source frame uncertainty to produce the uncertainty of the final science frame.

We used the science frame, together with its uncertainty and mask files as input to the SSC software SPICE, which produces a one-dimensional spectrum from a two-dimensional spectral image. To extract the spectra, we used the regular extraction mode, which equally weighs pixels when collapsing them along each row. We assumed a point source extraction, since the LH and SH apertures ($22''.3 \times 11''.1$ and $11''.3 \times 4''.7$, respectively) are likely to include the bulk of the NLR emission for most sources in our sample. The end product of SPICE is the wavelength and flux calibrated spectrum for each individual order.

We merged the spectra of the various orders to a single spectrum for each nod position, clipping noisy edges (between 2-25 pixels, depending on the order). This task was performed for both the SH and the LH datasets. The SH and LH spectra were then merged to produce the full-range spectrum per nod position. The final spectrum of each object was produced by averaging the one-dimensional, full-range spectra of the two nod positions. Special care was taken not to merge sky-subtracted and non-sky-subtracted datasets for sources with observations from different programs. At the wavelengths of key atomic/molecular lines, only nod positions without bad pixels were used, when possible. For all other pixels with a bad pixel flag in one nod position, we only kept the value of the second nod position when the two values differed by more than the local rms noise value.

3.2. Line Fitting

As in Dasyra et al. (2008)⁸, we fitted all lines and their underlying continua using Gaussian and second-order polynomial functions, respectively. Gaussian fitting was preferred over direct FWHM computations which, given the resolu-

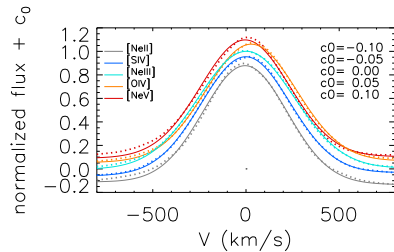


Fig. 2.— Stacked profiles (dotted lines) constructed using 29 $z < 0.02$ individual sources with unresolved line detections at all wavelengths. Solid lines correspond to the Gaussian best-fit solutions of the stacked profiles. The differences in the line peak positions are indicative of wavelength calibration uncertainties.

tion of IRS, can only be reliably performed for few high-velocity systems (e.g., Spoon & Holt 2009). Gaussian fitting also suits best the studies of cloud kinematics on virial, regular, or symmetric motions, instead of clouds that are entrained by asymmetric outflows (Greene & Ho 2005).

To claim a line detection, we required that its signal-to-noise ratio (S/N) was greater than 3. To measure line widths, however, we only used lines with $S/N > 5$ to avoid studying profiles of barely detected lines. We considered resolved all lines with $\sigma_m - \epsilon_m > \sigma_i + \epsilon_i$, where σ_m is the measured velocity dispersion, σ_i is the instrumental resolution at a given wavelength divided by 2.35, and ϵ_i is the error of σ_i . The average resolution value in the $12.0\text{--}18.0\text{ }\mu\text{m}$ range, which comprises all neon lines for the low z galaxies, is $507 \pm 66\text{ km s}^{-1}$. The $25.0\text{--}34.2\text{ }\mu\text{m}$ range, which comprises most of the O IV emission, has an average resolution of $503 \pm 63\text{ km s}^{-1}$. The error of σ_m , ϵ_m , encapsulates both measurement and instrumental uncertainties. It was computed as $(\epsilon_{st}^2 + \epsilon_i^2)^{0.5}$, where ϵ_{st} is the standard deviation of the different velocity dispersion values that were obtained for each line when using different polynomial functions to describe its underlying continuum. Intrinsic velocity dispersions, σ , were computed as $(\sigma_m^2 - \sigma_i^2)^{0.5}$, converted to restframe, and presented in Tables 1 and 2 for key fine-structure lines in all sources.

To assess possible systematic errors in the wavelength calibration, we normalized and stacked the line profiles of 29 sources with detected but unresolved emission lines of [Ne II], [S IV], [Ne III], [O IV], and [Ne V] (Figure 2). The stacking of un-

⁸All previously presented data were reanalyzed to account for changes in the *Spitzer* pipeline, and for enhancements in our bad-pixel identification routines.

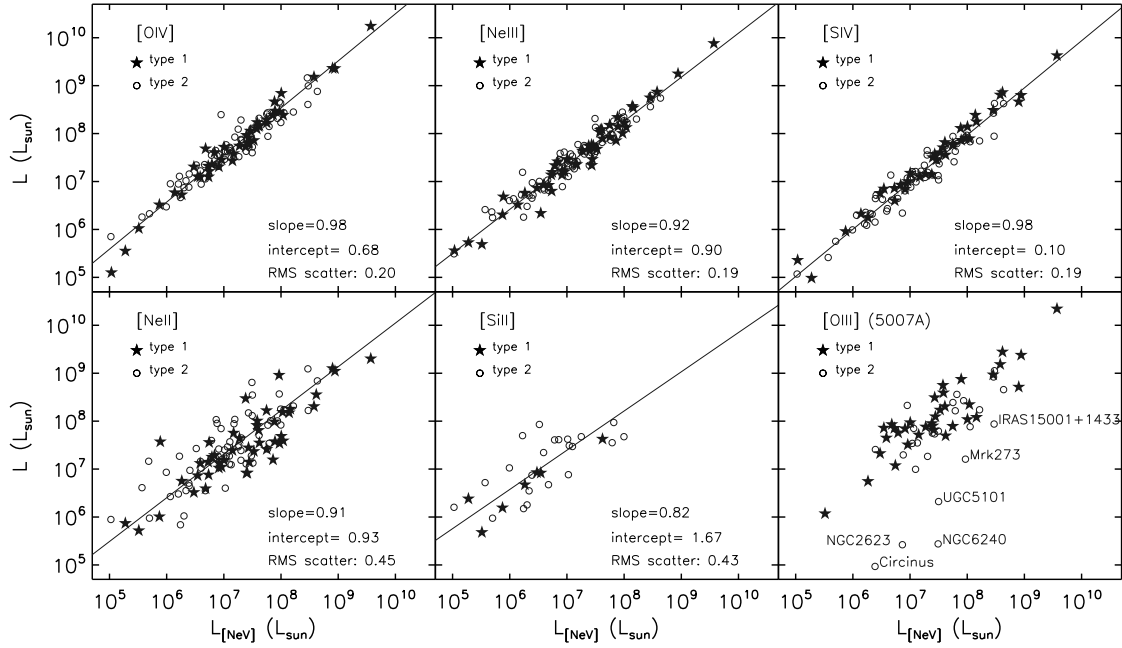


Fig. 3.— Relation of the [Ne V] luminosity, commonly used as an AGN indicator, with the luminosities of other fine-structure lines in MIR and optical wavelengths. The optical luminosities are not corrected for extinction.

resolved lines in different- z sources permitted for a finer sampling of the instrumental resolution curve than that determined by the detector pixel size. We only used sources at $z < 0.02$ to study systematic effects within a few pixels from the restframe wavelength of each line. This z cutoff translates to 25 pixels at the center of the SH array range, $14.7 \mu\text{m}$. We found that line peak offsets due to such systematics are typically limited to 50 km s^{-1} .

4. Results

4.1. Identifying NLR Tracers in the MIR

Of the 304 AGN in our sample, 300 had spectral coverage at $10.51 \mu\text{m}$, and 143 showed [S IV] emission. Similarly, 226 sources had spectral coverage at $25.89 \mu\text{m}$, and 135 had [O IV] detections. Thus, the typical line detection rate was of order $\sim 50\%$.

We plotted the luminosities of the most frequently observed MIR lines against that of [Ne V] to identify fine-structure lines that can be reliably used as tracers of the gas that is photoionized by the AGN (Figure 3). Given that photons of at least 97.12 eV are required to ionize Ne IV to Ne V,

its ionization source must be far-ultraviolet or soft X-ray radiation from the AGN. We find that the [Ne V] luminosity is on a tight correlation of 0.2 dex scatter with the [O IV] and [S IV] luminosities (Figure 3; Pereira-Santaella et al. 2010), and we further confirm that the [Ne V] and [Ne III] luminosities trace each other well (Gorjian et al. 2007). Therefore, the Ne V, O IV, Ne III, and S IV ions are most likely to be primarily excited by the same mechanism. However, the scatter between the luminosities of [Ne V] and [Ne II] or [Si II] is approximately twice as high, of 0.4–0.5 dex. Ne II and Si II have low ionization potentials (21.56 and 8.15 eV , respectively), thus, a non-negligible part of their line emission could be tracing star-forming regions in the AGN host galaxy.

The excellent, almost one-to-one correlation over several orders of magnitude in luminosity that is seen between the [Ne V] $14.32 \mu\text{m}$ and [S IV] $10.51 \mu\text{m}$ lines does not include any extinction correction. This result indicates that the bulk of the [S IV] emission is not strongly affected by the silicate absorption feature centered at $9.7 \mu\text{m}$, which is seen in several of our targets with moderate or high optical depths, i.e. $\tau > 0.5$. Thus,

the geometric distribution of the silicates is likely to be more compact than the size of the NLR (see also Soifer et al. 2002; Tristram et al. 2007; Schweitzer et al. 2008). While obscuration effects do not significantly affect the relative fluxes of MIR lines, the [O III] 5007 Å emission can suffer from strong extinction primarily in type 2 AGN (Figure 3).

4.2. Line Profiles: Velocity Dispersion of Different Ionized Gas Components

Our query for sources with resolved [S IV], [Ne III], [O IV], or [Ne V] lines resulted in 81 AGN with kinematic information of the NLR gas in the MIR (Figures 4 and 5). The different fine-structure lines that were used as primary tracers of clouds photoionized by the AGN often led to different σ measurements (Figures 4 and 5). Differences in the ionization potential of the various ionic species can play a major role in determining the observed line profiles, alongside with differences in the critical density for collisional de-excitation of the various transitions, and with light extinction by dust particles. We find the [Ne V] line to be often broader than lines from ions of lower ionization potential (e.g., Mrk590; Figures 4 and 5; Tables 3 and 4). A significant increase in the average velocity dispersion with increasing ionization potential is shown in Figures 6 and 7, as found for 16 sources with resolved profiles in all [Ne II], [O III], [S IV], [Ne III], [O IV], and [Ne V] lines. This result provides evidence for a stratification of the NLR clouds, i.e., for ions of high ionization being located nearer to the BH than ions of low ionization potential (Filippenko & Halpern 1984; Oliva et al. 1994; Ho 2009).

Radially dependent line widths will also be produced if the NLR has a gas density gradient increasing with proximity to the BH (Filippenko & Halpern 1984; Ferguson et al. 1997), which is not connected to a mean ionization level gradient. The line widths will be affected as the line fluxes from transitions of low critical density for collisional de-excitation, n_c , will be preferentially suppressed at dense environments. We observe no trend of σ with n_c (Figure 6), suggesting that the typical NLR gas densities are below n_c for the MIR transitions that we examined. The lack of dependence of the average σ on n_c demonstrates the power of MIR lines in probing the NLR kinematics. One

counter example to this statistical finding could be MCG-03-34-064. Because all of its neon lines have higher velocity dispersions than [O IV] and [S IV], its NLR density could be of order 10^4 hydrogen atoms per cubic centimeter.

Dust either mixed or outside the NLR gas clouds can lead to different extinction of lines at different λ (Groves et al. 2004; Winter et al. 2010). Because MIR lines are less affected by obscuration than optical lines, they could be probing clouds that are nearer to the BH, where obscuration is often higher. In this case, their widths could be broader than those of optical lines, in particular in type 2 AGN. Mrk273, NGC2623, and IRAS15001+1433 do have larger [O IV] than [O III] widths and low [O III]/[O IV] flux ratios (see Figure 3), but their [O III] and [S IV] or [Ne III] widths are in good agreement with each other. The comparable ionization potentials of O III, S IV, and Ne III, i.e., 35.12, 34.79, and 40.96 eV respectively, ascribe again any profile differences to ionization effects. We conclude that obscuration is not a common driver of differences in the profiles of optical and IR lines. The nuclear obscuration could be high enough to hide blue wings, associated with outflows moving away from the observer, even in IR wavelengths.

A simple comparison of the NLR gas velocity dispersion to that of the stars in the host galaxy shows that σ is not identical to σ_* (Figure 8). The gas velocity dispersion systematically exceeds that of the stars, with a large scatter between the two quantities. The average velocity dispersion excess is in the range 50-100 km s⁻¹ for all lines. The excess could be intrinsically higher, given that the optical observations had a slit width that was often an order of magnitude narrower than the IRS slit width. The origin of this excess could be related to either gas clouds that are accelerated by AGN-feedback mechanisms (Ho 2009), or to virialized gas clouds with a more compact spatial distribution than that of the stars, when probed by emission lines from ions of ionization potential $\gtrsim 35$ eV. High spatial resolution MIR spectroscopy of 8 local AGN indicated that the [S IV] emission is unresolved at a scale of 100 pc (Hönig et al. 2008), while NIR integral-field-unit data of Circinus showed that most of the [Si VI] and [Ca VIII] emission is unresolved at 4 pc (Müller Sánchez et al. 2006). This velocity dis-

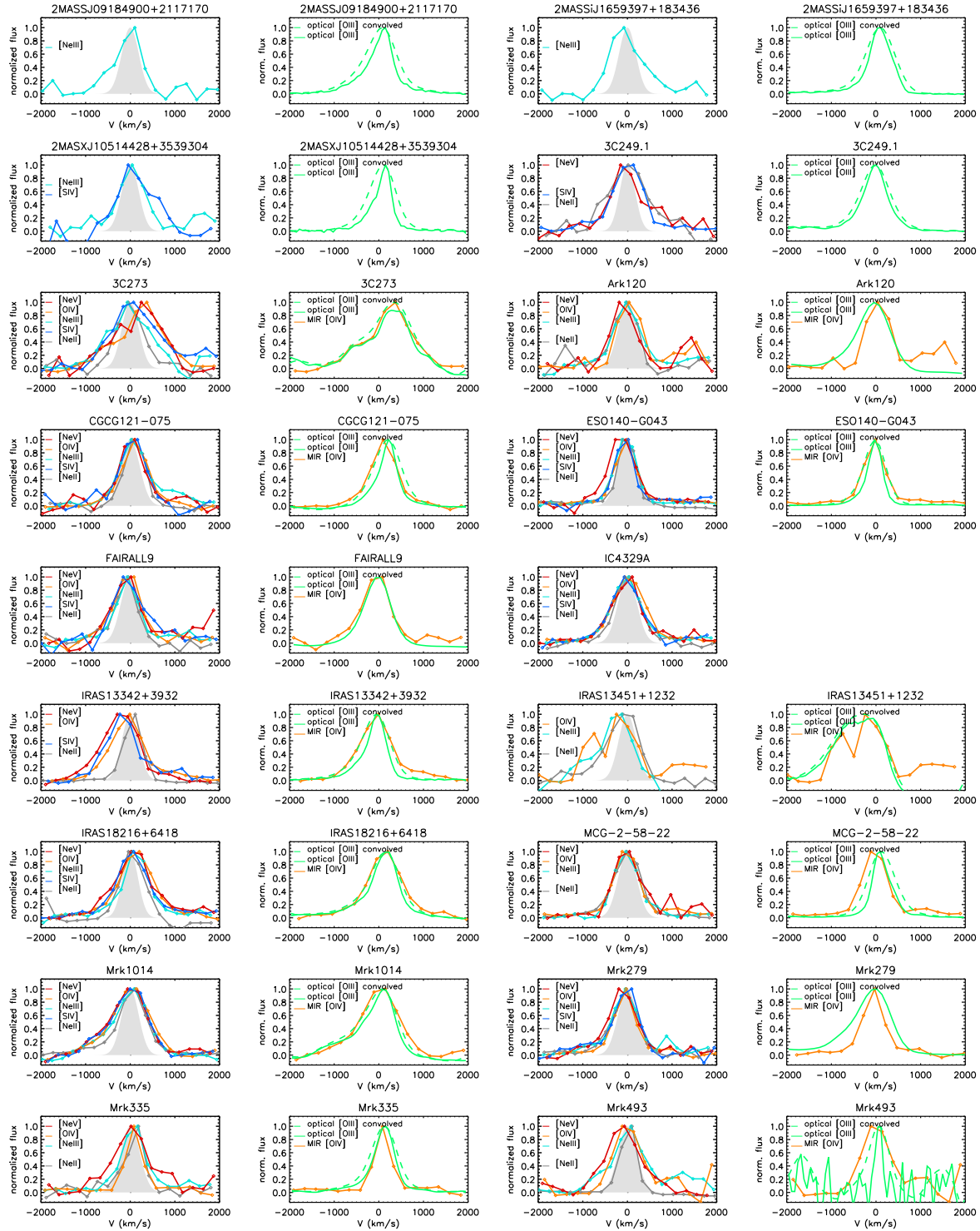


Fig. 4.— Profiles of fine-structure lines in type 1 AGN with at least one resolved NLR line in the MIR. For each source, the left panel presents the profiles of the MIR lines, while the right panel shows the comparison of the $[O\text{ IV}]$ $25.89\text{ }\mu\text{m}$ line with the optical $[O\text{ III}]$ $5007\text{ }\text{\AA}$ line, convolved to the resolution of the IRS data. The filled area corresponds to the average IRS resolution at the wavelengths of those lines.

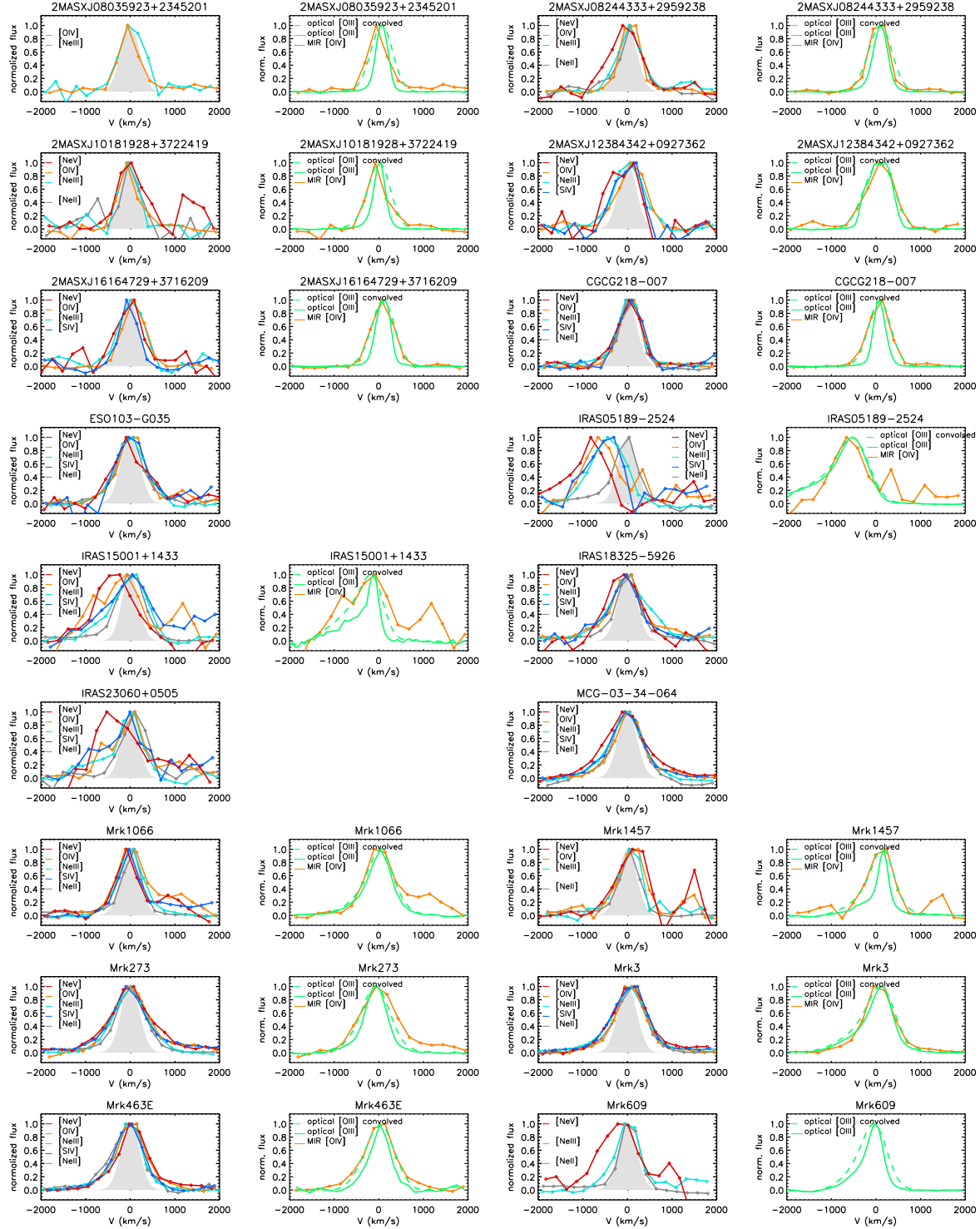


Fig. 5.— Profiles of fine-structure lines in type 2 AGN with at least one NLR line resolved in the MIR.

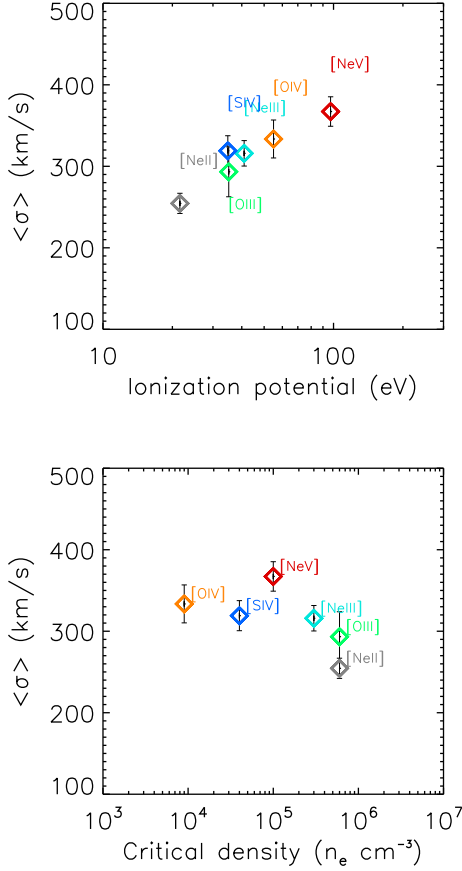


Fig. 6.— Average NLR gas velocity dispersion (corrected for instrumental broadening) as a function of ionization potential (upper panel) and critical density in units of electrons n_e per cubic centimeter (lower panel) for 16 sources with detections in all of the lines used for the construction of this figure.

persion excess is seen even for the [O III] 5007 Å line, which is resolved for all systems in our sample. Greene & Ho (2005) had also reported such an excess in a large flux-limited sample of AGN observed with SDSS.

Another trend known from optical NLR studies is that the widths of the lines increase with their own luminosities (Phillips et al. 1983; Whittle 1985, 1992b). We reproduce this result for the MIR fine-structure lines that we examined in Figure 9. The velocity dispersion correlates roughly as $L^{0.15}$ based on, e.g., the [Ne V] measurements. A higher dependence of σ on L is plausible when taking into account the upper limits of σ . An exact determi-

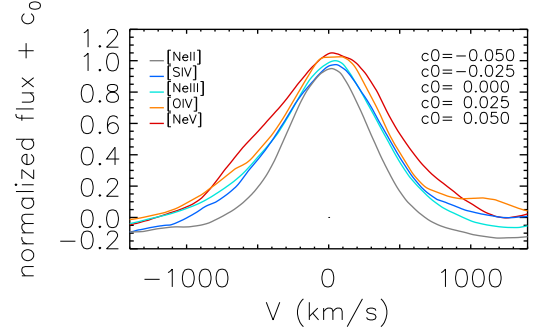


Fig. 7.— Stacked MIR line profiles of the 16 sources used in Figure 6.

nation of this slope will require the use of a flux-limited sample of AGN in the local universe.

4.3. Line Profiles: Shifts and Asymmetries

Changes in the profile moments of different lines can also be seen when the emission originates from gas out of dynamical equilibrium. Several of the 81 sources in our sample show signatures of outflowing (or inflowing) gas motions, such as an offset from systemic velocity. This offset often depends on the ionization potential of each ionic species. With increasing ionization potential, the lines trace clouds that are nearer to the BH, and therefore more susceptible to outflows. We identified 6 sources in which the offset between the peak of the lowest ionization line available and the highest ionization line available exceeds Nyquist sampling of the resolution element, $\gtrsim 250 \text{ km s}^{-1}$. Namely, these are the type 1 AGN 3C273, IRAS13342+3932, and the type 2 AGN IRAS05189-2524, IRAS15001+1433, IRAS23060+0505, and Mrk609 (see also Spoon et al. 2009; Spoon & Holt 2009). Line shifts below Nyquist sampling of the instrumental resolution, yet above the wavelength calibration uncertainty (50 km s^{-1}), could also be theoretically observed. They could be considered real if they systematically increased as a function of the ionization potential of the ionic species. Only one source⁹

⁹Other sources, such as NGC2623, NGC7469, Arp148, and PG1211+143, could also have outflows of ionized gas, which need to be proven with spectroscopy of higher resolution than that of IRS. The blue wings of [Ne V] and [O IV] in

satisfies this criterion, Mrk1457. Its [Ne V] and [Ne II] lines are offset by 100 km s^{-1} .

Asymmetric wings are found in $\sim 1/5$ th of the sources with resolved profiles. We consider such wings to be reliable only when they are detected in two or more lines. Similar [O III] 5007 \AA and [Ne III] or [Ne V] wings are observed, for example, in PG1351+640, PG1411+442, and PG1440+356. Likewise, an agreement of the [O III] and [O IV] $25.89 \mu\text{m}$ line profiles is found for 3C273, IRAS13451+1232, IRAS15001+1433, Mrk1014, NGC4235, and NGC7674. Specifically, IRAS13451+1232 is a merging system with two nuclei separated by $\sim 5 \text{ kpc}$ (e.g., Axon et al. 2000; Dasyra et al. 2006a). The velocity of the secondary [O IV] peak, at $\sim -1000 \text{ km s}^{-1}$, is comparable to the velocities of the outflowing [O I] and [O III] gas components that are seen in optical spectroscopy and that are associated with the nucleus responsible for the radio-jet emission (Holt et al. 2003).

5. Discussion

5.1. A Three Dimensional Plane connecting M_{BH} , and the L and σ of the NLR?

By performing a similar profile analysis of the [Ne V] and [O IV] lines, restricted only to AGN with direct M_{BH} measurements from reverberation experiments (Peterson et al. 2004), we previously demonstrated that the NLR velocity dispersion correlates with the mass of its central BH (Dasyra et al. 2008). We now further populate this relation using data from the full *Spitzer* archive, complementing them with ISO SWS data to cover the parameter space $\sigma \lesssim 200 \text{ km s}^{-1}$. The M_{BH} values for this expanded sample include single-epoch optical spectroscopic estimates for type 1 AGN, as well as direct M_{BH} measurements for a few type 2 AGN (see Section 2; Tables 3 and 4).

The fit to these data (Figure 10) was performed with the IDL routine MPFITFUN. Given the sparsity of data at the low σ end, we opted for a linear fit of fixed slope in logarithmic space.

NGC6240 are also redshifted with respect to [Ne II] and [Ne III], but their overall line shifts are hard to determine as these lines are blended with [Cl II] and [Fe II] (see also Armus et al. 2006).

The slope was set to 4.24, which is identical to that of the stellar relation (Ferrarese & Merritt 2000; Gebhardt et al. 2000) as recently revisited by Gültekin et al. (2009). While the rms scatter was computed using all available datapoints, the best-fit solution was computed using only *Spitzer* observations of sources with $M_{\text{BH}} > 10^7 M_{\odot}$ or ISO observations, as in Dasyra et al. (2008). The reason why we excluded *Spitzer* datasets for $M_{\text{BH}} < 10^7 M_{\odot}$ is that they would introduce a bias toward high intercept values: the resolution of IRS is insufficient to resolve lines on the left-hand side of the $M_{\text{BH}} - \sigma$ relation below this threshold. This excludes the type 2 AGN NGC1068, and the narrow-line Seyfert 1s (NLS1s) Mrk493, and NGC4051 that have high σ values for their BH masses. The existence of such outliers nonetheless suggests that σ could fail as a proxy of M_{BH} , as it is also known for the BLR gas (e.g., Vestergaard & Peterson 2006). On the other hand, such sources are not outliers in the relation connecting M_{BH} to the luminosity of the NLR lines (Figure 11).

The multiple relations between M_{BH} and σ , σ and L , and M_{BH} and L could be suggestive of a plane connecting these three parameters (Figure 12), which we fit using the equation

$$\log(M_{\text{BH}}) = \alpha \log(\sigma) + \beta \log(L) + \gamma, \quad (1)$$

where α, β , and γ are constants. We find that the best-fit-solution coefficients correspond to $\alpha=0.9$ and $\beta=0.5$, when averaged over all MIR lines. Given the L and $\sigma \sim^7$ proportionality shown in Figure 9, this result roughly reproduces the $M_{\text{BH}} \sim \sigma^4$ relation. In Figure 13, we present the plane equation for each line, when fixing the $\log(\sigma)$ and $\log(L)$ slopes to their average values for simplicity¹⁰. We find that the use of a plane equation minimizes the scatter of the NLR-based M_{BH} estimates from their actual values. The improvement primarily originates from the correction of the $M_{\text{BH}} - \sigma$ relation outliers at its low- M_{BH} and high- σ end.

¹⁰ We have adapted this approach throughout all fitting procedures in this work (see also Figures 10 and 11) to facilitate comparisons of the rms scatter among the various relations, and to avoid biases related to the small galaxy sample that is used for their creation and that varies from line to line.

5.2. The Origin of the Scaling Relations between the NLR Gas Properties and M_{BH}

The physical interpretation of the suggested plane linking the NLR line luminosity, velocity dispersion and the BH mass, varies depending upon the assumed kinematics and distribution of the gas clouds. A plane equation can be meaningful for clouds on accelerated motions powered directly by the AGN, via radiation pressure (Murayama & Taniguchi 1998) acting mostly upon dust particles due to their high opacity (Dopita et al. 2002), magnetic fields related to jets (Whittle 1992c), and AGN-related winds. The winds can lead to either asymmetric outflows, identified in 7% of the systems in this sample, or to symmetric outflows that can be related to the AGN accretion disk (Crenshaw et al. 2003; Ho 2009). In this scenario, the measured gas velocity would be related to the fraction of the energy generated by the AGN that is deposited into the NLR gas. The luminosity would be a probe of the AGN accretion rate, since the luminosities of MIR NLR lines are known to be correlated with the optical, X-ray, and bolometric AGN luminosities (Schweitzer et al. 2006; Dasyra et al. 2008; Meléndez et al. 2008; Rigby et al. 2009; R. Mor et al. in preparation). A plane connecting σ , L , and M_{BH} would then suggest that the kinetic energy of the interstellar medium (ISM), as measured from the MIR lines, is directly related to the amount of material that is accreted onto the BH for a given M_{BH} value. An analogous idea was introduced by Merloni et al. (2003), who found a correlation between the mass of an accreting BH with its X-ray and radio luminosities.

Instead of responding to AGN feedback mechanisms, the gas clouds could be in virial motions that are dictated by the enclosed mass at the NLR radius R . For a geometric factor f converting this total mass to the BH mass, the virial equation can be written as

$$\log(M_{\text{BH}}) = 2\log(\sigma) + \log(R) + \log(f) - \log(G), \quad (2)$$

where G is the gravitational constant. In this model, the NLR radius depends on the AGN luminosity alongside with the stellar mass and distribution in the AGN host galaxy. Equation (2) will take the form of Equation (1) if R scales with the AGN luminosity as a power law of L , as found

for the [O III] 5007 Å line (Bennert et al. 2002; Schmitt et al. 2003). The hardness of the ionizing radiation together with the ionization fraction, the covering factor, and the density distribution of the clouds can also determine how far the AGN radiation reaches, illuminates, and photoionizes gas clouds. For example, the observed increase of σ with L can be driven either by a tendency for more massive BHs to reside in larger galaxies (Ho 2009), or by the ionization state of the NLR. Lines from ions of high ionization potential are thought to be tracing matter-bound clouds that are partially ionized (Murayama & Taniguchi 1998; Wilson et al. 1997). In the case of partially ionized clouds, an increase of the AGN luminosity can lead to an overall expansion of the NLR, while most of the ionization can still occur for clouds at small radii. The exact relation between σ , L , and M_{BH} will depend on the gas density distribution, which is encapsulated in the scaling factor f . The coefficients of the best-fit plane solution, $\alpha=0.9$ and $\beta=0.5$, suggest that f is dropping with σ , corresponding to a lower scaling factor for denser gas within a fixed radius. If however, the scaling factor f was constant, α would be equal to 2, and the best-fit plane solution would correspond to $\beta=0.4$. Such a solution could also be plausible. It would increase the rms scatter by a small amount, i.e., by only 0.01–0.02 dex for the MIR lines and by 0.07 dex for [O III].

If the cloud kinematics cannot be approximated by either feedback-driven motions or by virial motions, Equation 1 might not provide a good means of estimating M_{BH} . For cloud kinematics that are described by a combination of virial and accelerated motions, e.g., in a virialized NLR where radiation pressure is significant, M_{BH} is proportional to $\sigma^2 R G^{-1} + a' L$, where a' is a constant that depends on the column density and level of ionization of the clouds (Marconi et al. 2008; but see also Netzer & Marziani 2010). Further investigation of the optimal description of M_{BH} from narrow line properties will be tested on large, flux-limited samples of AGN with multiwavelength datasets. This will be the focus of a forthcoming paper using SDSS data.

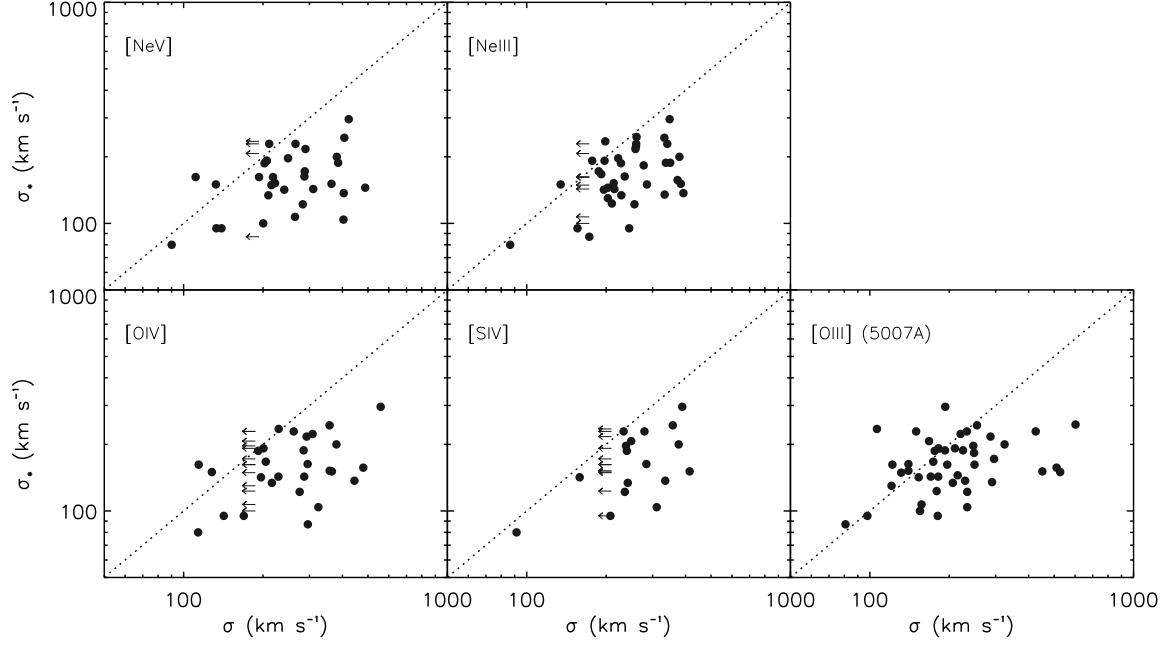


Fig. 8.— Comparison of the stellar velocity dispersion with the NLR gas velocity dispersion, as measured from MIR lines and from the optical [O III] 5007 Å line.

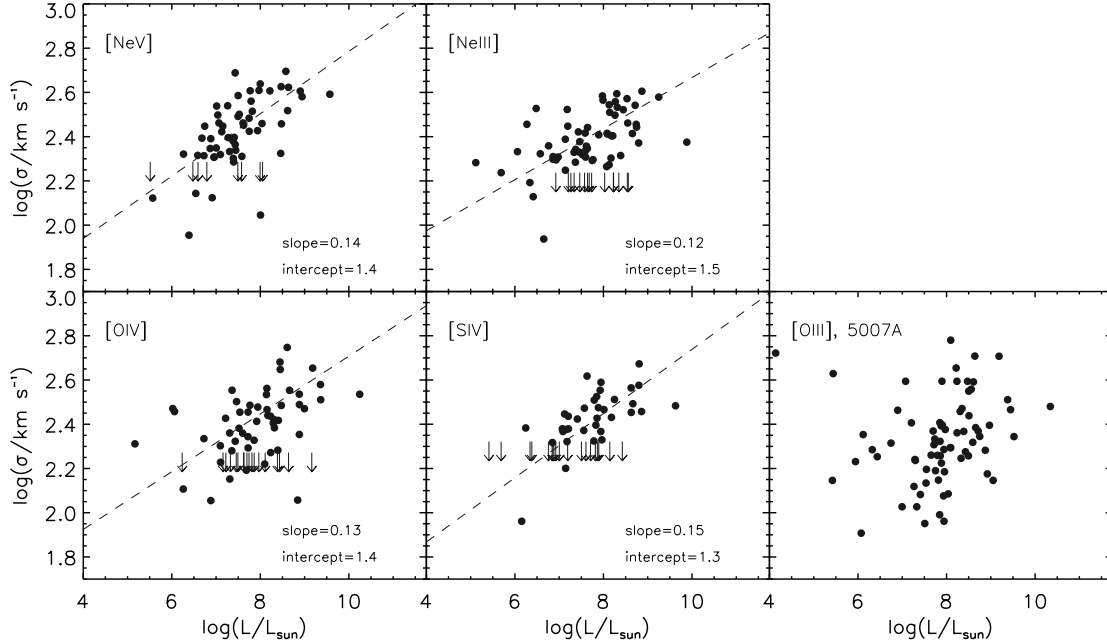


Fig. 9.— Velocity dispersion increase with the luminosity of the line from which it was measured. The error-weighted best-fit solution for each MIR line is presented with a dashed line.

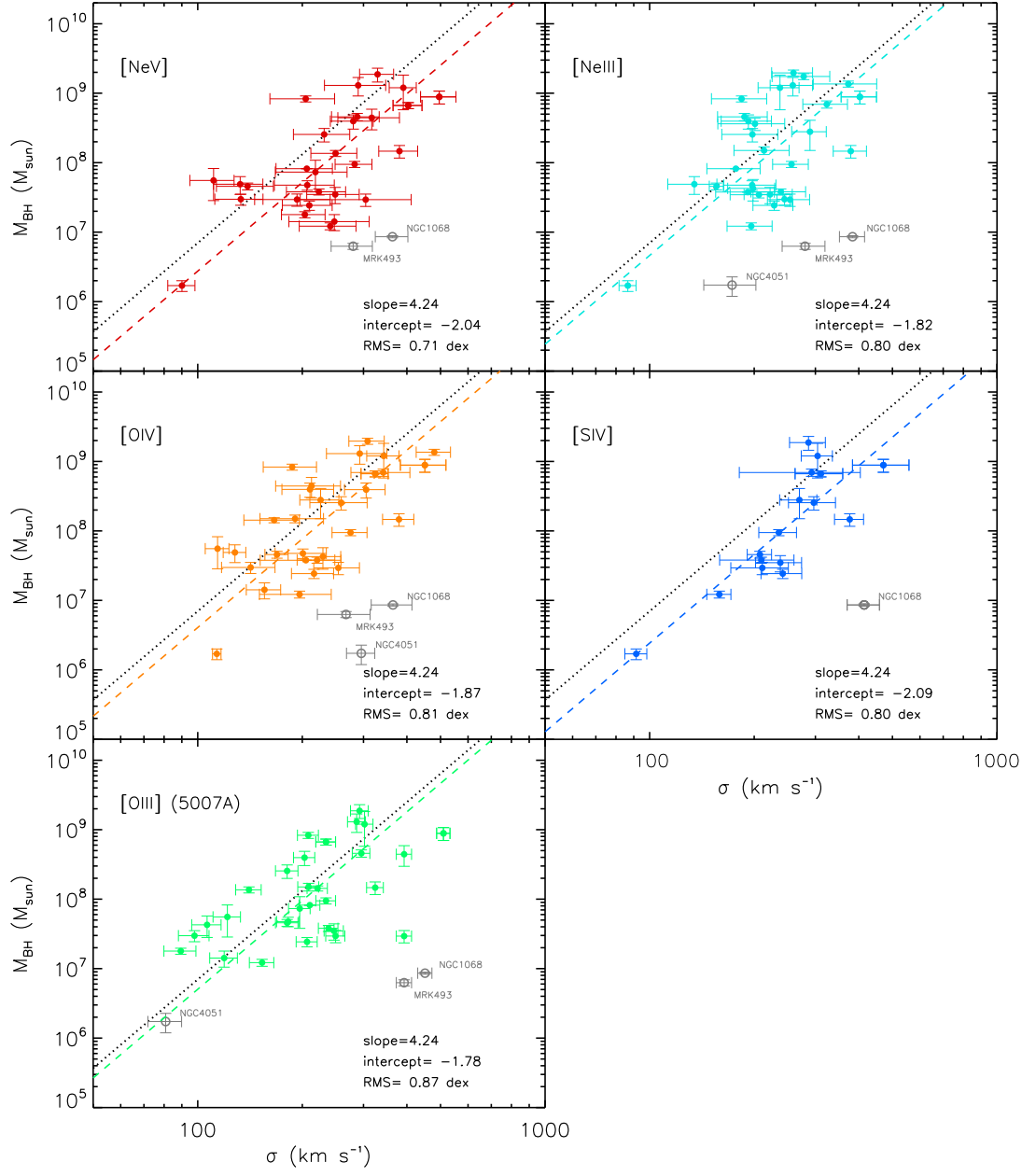


Fig. 10.— M_{BH} vs NLR velocity dispersion. Open circles correspond to sources included in the rms computation, but excluded from the fit due to the lack of corresponding *Spitzer* data for the left-hand side of the relation. The best-fit solution to all other data points is presented with a dashed line. The dotted line corresponds to the Gültekin et al. (2009) relation, thought appropriate for the velocity dispersion of the stars in the bulge.

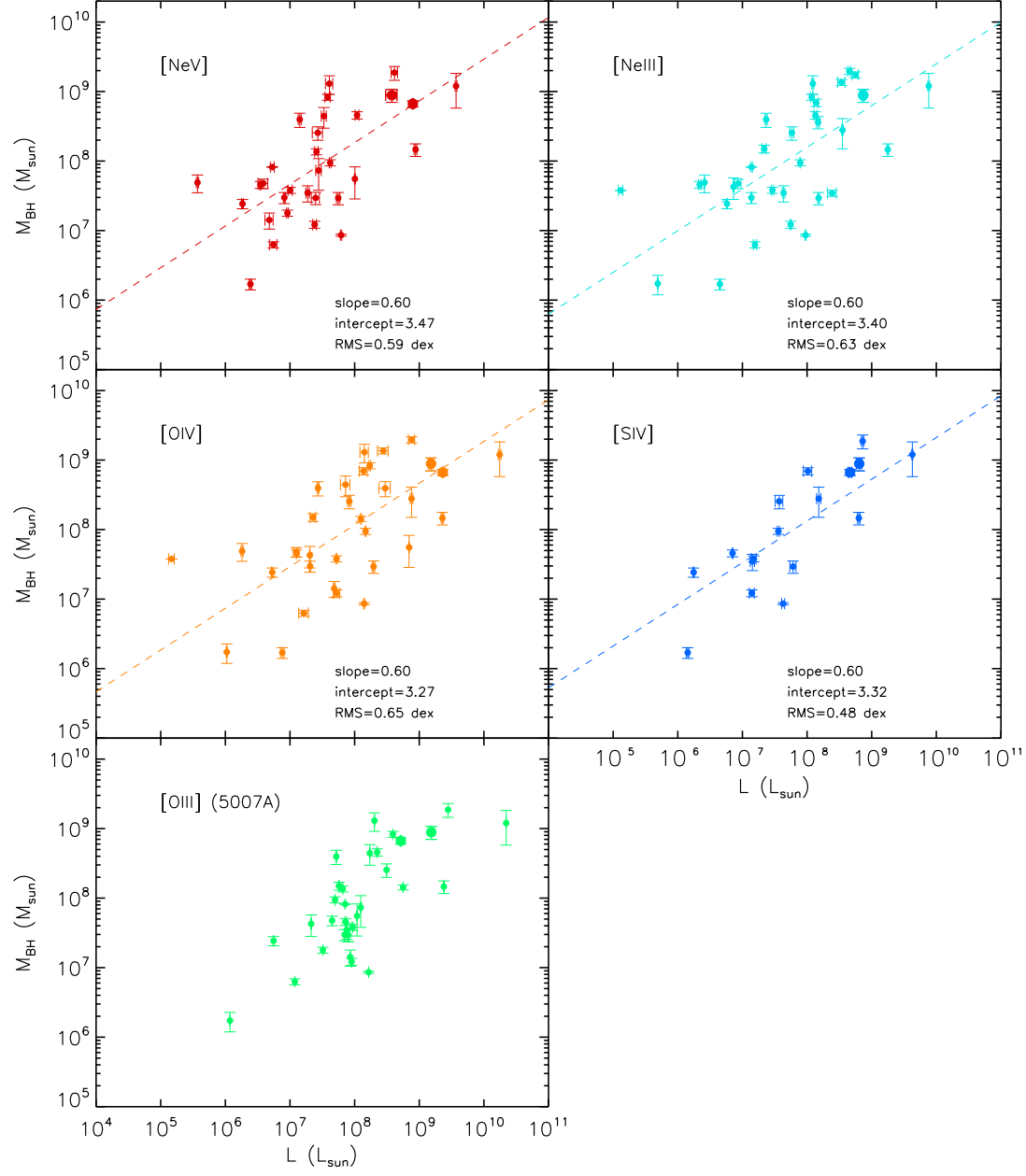


Fig. 11.— M_{BH} vs narrow line luminosity relation.

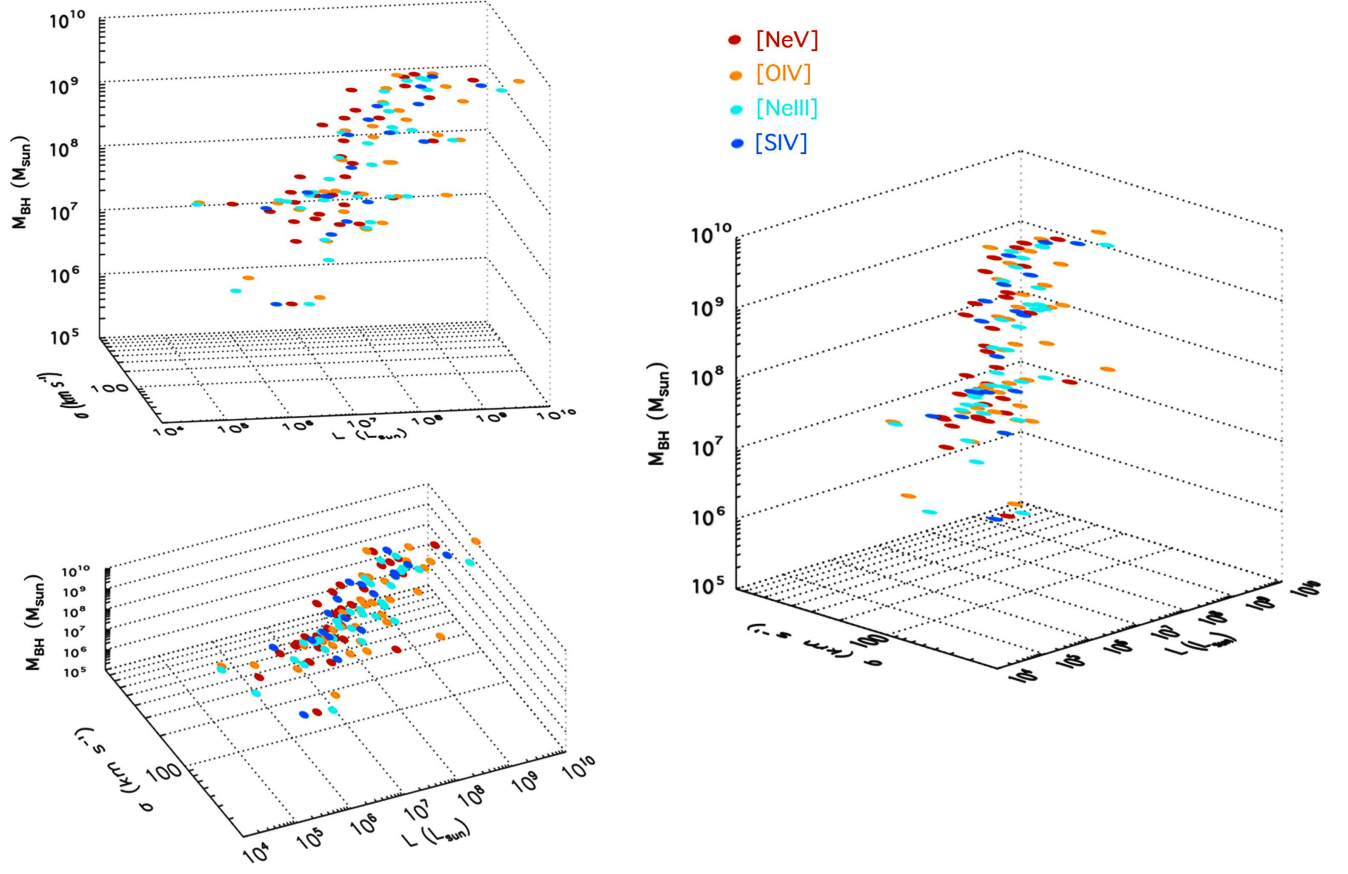


Fig. 12.— Different views of the plane suggested to connect M_{BH} , and the velocity dispersion and luminosity of AGN narrow lines in the MIR.

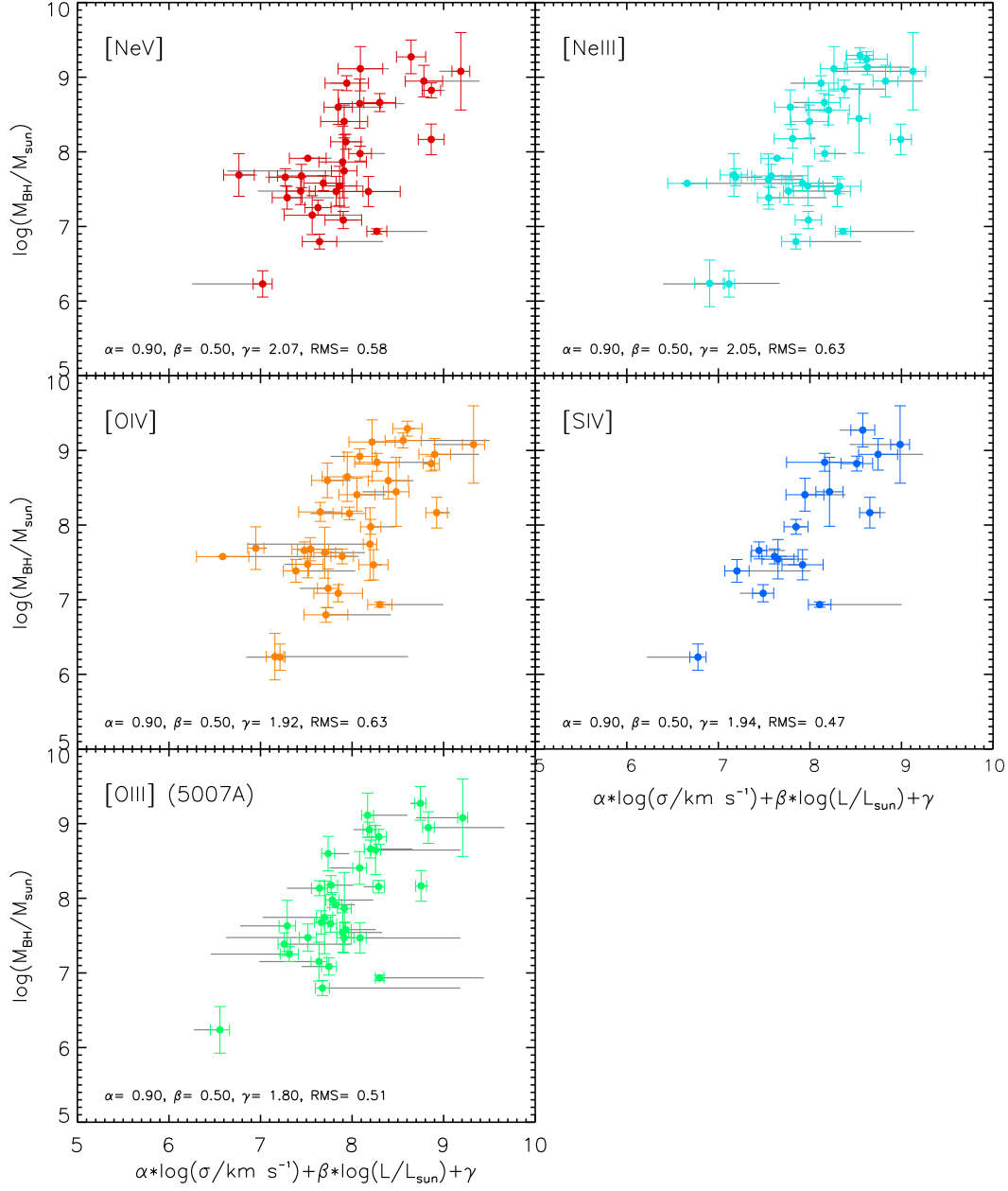


Fig. 13.— Linear combination, i.e., plane equation, of $\log(\sigma)$ and $\log(L)$ that describes $\log(M_{\text{BH}})$. The horizontal solid lines indicate where each source would have been located if its M_{BH} was estimated from the $M_{\text{BH}} - \sigma$ relation (Figure 10) instead.

5.3. Black Hole Mass Estimates in Obscured AGN

Given that we see no significant difference in the NLR properties of type 1 and type 2 AGN at a given L or σ_* (see also Pereira-Santaella et al. 2010), we applied the relations presented earlier in this work to type 2 AGN for which such an analysis is presently possible from *Spitzer* data. Only four of these sources have other, direct M_{BH} measurements (Table 2). The comparison between the M_{BH} estimates from the stellar $M_{\text{BH}} - \sigma_*$ relation, the $M_{\text{BH}} - \sigma$ relation for the NLR gas, and the best-fit linear combination of $\log(\sigma)$ and $\log(L)$ are presented in Table 5. For either computation based on the NLR gas, the result is averaged over all available MIR lines. We find that the median ratio of M_{BH} as estimated from the plane equation over M_{BH} as estimated from the stellar velocity dispersion is 1.8. On the other hand, the median ratio of M_{BH} as estimated from the NLR gas velocity dispersion over M_{BH} as estimated from the stellar velocity dispersion is much higher, 6.5. The difference seen when folding a luminosity dependence on the computation of M_{BH} is largest for the IR-bright galaxies IRAS05189-2524, IRAS15001+1433, and Mrk609, which have gas motions that are predominantly out of dynamical equilibrium.

6. Conclusions

We queried the full *Spitzer* archive for high-resolution IRS spectra of type 1 AGN with BLR-based M_{BH} estimates from optical spectroscopy, and type 2 AGN. We analyzed the spectra of 298 objects, which we combined with ISO spectra of 6 more AGN, aiming to study the fundamental properties of the NLR in the IR, and to calibrate its fine-structure-line widths and luminosities to the mass of the central black hole. We found the following.

- All of the [Ne V], [O IV], [Ne III], and [S IV] line luminosities are well correlated with each other (with an rms scatter of ~ 0.2 dex). Given the high ionization potential of Ne IV to Ne V, their emission is attributed to (further) photoionization of ions by the AGN. Thus, all of these lines can be used to study the NLR kinematics.
- The bulk of the silicates responsible for the $9.7 \mu\text{m}$ absorption feature is likely to be located in a region smaller than the NLR. Otherwise, the luminosity of [S IV] at $10.51 \mu\text{m}$ would not correlate equally well with that of all other IR narrow lines without an extinction correction in obscured AGN.
- Of the 304 sources in our sample, 81 had at least one [Ne V], [O IV], [Ne III], or [S IV] narrow line that was resolved. We find that, on average, the line widths increase with increasing ionization potential of the species that emit them in the range 22–97 eV. Different fine-structure lines probe different (locations within the) clouds, with high-ionization-potential ions being preferentially found nearer to the BH.
- No trend was observed between the line width and critical density for these transitions, indicating that the average density of the NLR gas is typically below 10^4 hydrogen atoms per cubic centimeter.
- The velocity dispersions of all MIR lines that we examined, as well as that of the [O III] 5007 \AA line, are systematically above the velocity dispersion of the stars in the AGN host galaxies. Moreover, the line widths increase with their own luminosities, as known from optical wavelengths.
- The mass of the central BH correlates with the velocity dispersion and with the luminosity of the NLR lines. We speculate that these results could be suggestive of a three-dimensional plane, connecting $\log(M_{\text{BH}})$ to a linear combination of $\log(\sigma)$ and $\log(L)$. Such a plane equation could be meaningful for a virial distribution in which the NLR radius has a power-law dependence on the AGN luminosity, or for AGN-feedback driven motions.
- Given that we find no significant differences in the NLR kinematic properties of type 1 and type 2 AGN, we used the NLR gas properties as seen in the MIR to estimate the BH masses residing in 35 local obscured AGN.

K. D. acknowledges support by the European Community through a Marie Curie Fellowship (PIEF-GA-2009-235038) awarded under the Seventh Framework Programme (FP7/2007-2013). The authors wish to thank T. Boroson and B. Peterson for providing optical spectra to be compared with the MIR ones, and S. Collin for useful discussions. This work made use of the NASA Extragalactic Database, and it was based on archival data obtained with the *Spitzer* Space Telescope, operated by the Jet Propulsion Laboratory, California Institute of Technology under a contract with NASA.

REFERENCES

- Armus, L., et al. 2006, ApJ, 640, 204
- Axon, D. J., Capetti, A., Fanti, R., Morganti, R., Robinson, A., & Spencer, R. 2000, AJ, 120, 2284
- Baldwin, J., Philips, M., & Terlevich, R., 1981, PASP, 93, 5
- Bassani, L., Dadina, M., Maiolino, R., Salvati, M., Risaliti, G., della Ceca, R., Matt, G., & Zamorani, G. 1999, ApJS, 121, 473
- Bennert, N., Falcke, H., Schulz, H., Wilson, A. S., & Wills, B. J. 2002, ApJ, 574, L105
- Bennert, N., Barvainis, R., Henkel, C., & Antonucci, R. 2009, ApJ, 695, 276
- Bentz, M. C., et al. 2006, ApJ, 651, 775
- Bentz, M. C., et al 2009, ApJ, 705, 199
- Blandford, R. D. & McKee, C. F. 1982, ApJ, 255, 419
- Boroson, T. A., & Green, R. F. 1992, ApJS, 80, 109
- Cappellari, M., Neumayer, N., Reunanen, J., van der Werf, P. P., de Zeeuw, P. T., & Rix, H.-W. 2009, MNRAS, 394, 660
- Crenshaw, D. M., Kraemer, S. B., & George, I. M. 2003, ARA&A, 41, 117
- Dasyra, K. M., Tacconi, L. J., Davies, R.I., Lutz, D., Genzel, R., Burkert, A., Veilleux, S. & Sanders, D. 2006, ApJ 638, 745
- Dasyra, K. M., et al. 2006, ApJ, 651, 835
- Dasyra, K. M., et al. 2007, ApJ, 657, 102
- Dasyra, K. M., et al. 2008, 674, L9
- Denney, K. D., et al. 2010 ApJ, 721, 715
- Dopita, M. A., Groves, B. A., Sutherland, R. S., Binette, L., Cecil, G. 2002, ApJ, 572, 753
- Falcon-Barroso, J., et al., 2006, MNRAS, 369, 529
- Ferguson J. W., Korista, K. T., Baldwin, J. A., & Ferland, G. J. 1997, ApJ 487, 122
- Ferrarese, L., & Merritt, D. 2000, ApJ, 539, L9
- Filippenko A. V., & Halpern, J. P. 1984, ApJ, 285, 458
- Gebhardt, K. et al. 2000, ApJ, 539, L13
- Genzel, R., Eckart, A., Ott, T., & Eisenhauer, F. 1997, MNRAS, 291, 219
- Gilli, R., Comastri, A., & Hasinger, G. 2007, A&A, 463, 79
- Greene, J. E., & Ho L. C. 2005, ApJ, 627, 721
- Greenhill, L. J., et al. 2003, ApJ, 590, 162
- Groves B. A., Dopita, M. A., & Sutherland, R. S. 2004, ApJS, 153, 9
- Gorjian, V., Cleary, K., Werner, M. W., & Lawrence, C. R. , 2007, ApJ, 655, L73
- Gültekin, K., et al. 2009, ApJ, 698, 198
- Hao, L., et al. 2005, AJ, 129, 1795
- Harms, R. J., et al. 1994, ApJ, 435, L35
- Heckman, T. M., van Breugel, W. J. M., Miley, G. K., & Butcher, H. R. 1983, AJ, 88, 1077
- Herrnstein, J. R., Moran, J. M., Greenhill, L. J., & Trotter, A. S. 2005, ApJ, 629, 719
- Hinz, J. L., & Rieke, G. H., 2006, ApJ, 646, 872
- Ho, L. C., Filippenko, A. V., & Sargent, W. L. W. 1997, ApJS, 112, 315
- Ho, L. C., Filippenko, A. V., & Sargent, W. L. W. 1997, ApJ, 487, 568

- Ho, L. C. 2007, *ApJ*, 668, 94
- Ho, L. C. 2009, *ApJ*, 699, 638
- Ho, L. C. & Kim, M. 2009, *ApJS*, 184, 398
- Holt, J., Tadhunter, C. N., & Morganti, R. 2003, *MNRAS*, 342, 227
- Hönig, S. F., Smette, A., Beckert, T., Horst, H., Duschl, W., Gandhi, P., Kishimoto, M., & Weigelt, G. 2008, *A&A*, 485, L21
- Houck, J., et al. 2004, *ApJS*, 154, 18
- Kauffmann, G., et al. 2003, *MNRAS*, 346, 1055
- Kaspi, S., Smith, P. S., Netzer, H., Maoz, D., Januzzi, B. T., Giveon, U. 2000, *ApJ*, 533, 631
- Kaspi, S., Brandt, W. N., Maoz, D., Netzer, H., Schneider, D. P., & Shemmer, O. 2007, *ApJ*, 659, 997
- Kewley, L. J., Groves, B., Kauffmann, G., & Heckman, T. 2006, *MNRAS* 372, 961
- Kim, M., Ho, L. C., Peng, C. Y., Barth, A. J., Im, M., Martini, P., & Nelson, C. H. 2008, *ApJ*, 687, 767
- Lacy, M., et al. 2007, *AJ*, 133, 186
- Laor, A. 2007, *ASPC*, 373, 384
- Liu, X., Zakamska, N. L., Greene, J. E., Strauss, M. A., Krolik, J. H., & Heckman, T. M. 2009, *ApJ*, 702, 1098
- Lodato, G., & Bertin, G. 2003, *A&A*, 398, 517
- Macchetto, F., Marconi, A., Axon, D. J., Capetti, A., Sparks, W. B., & Crane, P. 1997, *ApJ*, 489, 579
- Marconi, A., Risaliti, G., Gilli, R., Hunt, L. K., Maiolino, R., & Salvati, M. 2004, *MNRAS*, 351, 169
- Marconi, A., Axon, D. J., Maiolino, R., Nagao, T., Pastorini, G., Petrini, P., Robinson, A., & Torricelli, G. 2008, *ApJ*, 678, 693
- Marziani, P., Sulentic, J. W., Zamanov, R., Calvani, M., Dultzin-Hacyan, D., Bachev, R., & Zwitter, T. 2003, *ApJS*, 145, 199
- Meléndez, M., et al. 2008, *ApJ*, 682, 94
- Merloni, A., Heinz, S., & di Matteo, T. 2003, *MNRAS*, 345, 1057
- Merloni, A., Rudnick, G., & di Matteo, T. 2004, *MNRAS*, 354, L37
- Miyoshi, M., Moran, J., Herrnstein, J., Greenhill, L., Nakai, N., Diamond, P., & Inoue, M. 1995, *Nature*, 373, 127
- Mulchaey, J. S., Koratkar, A., Ward, M. J., Wilson, A. S., Whittle, M., Antonucci, R. R. J., Kinney, A. L., & Hurt, T. 1994, *ApJ*, 436, 586
- Müller Sánchez, F., Davies, R. I., Eisenhauer, F., Tacconi, L. J., Genzel, R., & Sternberg, A. 2006, *A&A*, 454, 481
- Murayama, T., Taniguchi, Y., & Iwasawa, K. 1998, *AJ*, 115, 460
- Murayama, T. & Taniguchi, Y. 1998, *ApJ*, 497, L9
- Nelson, C. H., & Whittle, M. 1996, *ApJ*, 465, 96
- Nelson, C. H. 2000, *ApJ*, 554, L91
- Nelson, C., Green, R. F., Bower, G., Gebhardt, K., & Weistrop, D. 2004, *ApJ*, 615, 652
- Netzer, H. 2004, *IAUS*, 222, 389
- Netzer, H., & Trakhtenbrot, B. 2007, *ApJ*, 654, 754
- Netzer, H., & Marziani, P. 2010, *ApJ*, 724, 318
- Neumayer, N., Cappellari, M., Reunanen, J., Rix, H.-W., van der Werf, P. P., de Zeeuw, P. T., & Davies, R. I. 2007, *ApJ*, 671, 1329
- Oliva, E., Salvati, M., Moorwood, A. F. M., & Marconi, A. 1994, *A&A*, 288, 457
- Onken, C. A., Ferrarese, L., Merritt, D., Peterson, B. M., Pogge, R. W., Vestergaard, M., & Wandel, A. 2004, *ApJ* 615, 645
- Pahre, M. A. 1999, *ApJS*, 124, 127
- Pereira-Santaella, M., Diamond-Stanic, A. M., Alonso-Herrero, A., & Rieke, G. H. 2010, *ApJ*, 725, 2270

- Peterson, B. M. 1993, *PASP*, 105, 247
- Peterson, B. M., et al. 2004, *ApJ*, 613, 682
- Phillips, M. M., Charles, P. A., & Baldwin, J. A. 1983, *ApJ*, 266, 485
- Reyes, R., et al. 2008, *AJ*, 136, 2373
- Rigby, J. R., Diamond-Stanic, A. M., & Aniano, G. 2009, *ApJ*, 700, 1878
- Shields, G. A., Gebhardt, K., Salviander, S., Wills, B. J., Xie, B., Brotherton, M. S., Yuan, J., & Dietrich, M. 2003, *ApJ*, 583, 124
- Schmitt, H. R., Antonucci, R. R. J., Ulvestad, J. S., Kinney, A. L., Clarke, C. J., & Pringle, J. E. 2001, *ApJ*, 555, 663
- Schmitt, H. R., Donley, J. L., Antonucci, R. R. J., Hutchings, J. B., & Kinney, A. L. 2003, *ApJS*, 148, 32
- Schweitzer, M., et al. 2006, *ApJ*, 649, 79
- Schweitzer, M., et al. 2008, *ApJ*, 679, 101
- Soifer, B. T., Neugebauer, G., Matthews, K., Egami, E., & Weinberger, A. J. 2002, *AJ*, 124, 2980
- Spinelli, P. F., Storchi-Bergmann, T., Brandt, C. H., & Calzetti, D. 2006, *ApJS*, 166, 498
- Spoon, H. W. W., Armus, L., Marshall, J. A., Bernard-Salas, J., Farrah, D., Charmandaris, V., & Kent, B. R. 2009, *ApJ*, 693, 1223
- Spoon, H. W. W., & Holt, J. 2009, *ApJ*, 702, L42
- Sturm, E., Lutz, D., Verma, A., Netzer, H., Sternberg, A., Moorwood, A., Oliva, E., & Genzel, R. 2002, *A&A*, 393, 821
- Tacconi, L. J., Genzel, R., Lutz, D., Rigopoulou, D., Baker, A. J., Iserlohe, C., & Tecza, M. 2002, *ApJ*, 580, 73
- Tecza, M., Genzel, R., Tacconi, L. J., Anders, S., Tacconi-Garman, L. E., & Thatte, N. 2000, *ApJ*, 537, 178
- Tristram, K. R. W., et al. 2007, *A&A*, 474, 837
- Turner, T. J., George, I. M., Nandra, K., & Mushotzky, R. F. 1997, *ApJS*, 113, 23
- Veilleux, S., Kim, D.-C., Sanders, D. B., Mazzarella, J. M., & Soifer, B. T. 1995, *ApJS*, 98, 171
- Veilleux, S., Kim, D.-C., & Sanders, D. B. 1999, *ApJ*, 522, 113
- Vestergaard, M., & Peterson, B. M. 2006, *ApJ*, 641, 689
- Whittle, M. 1985, *MNRAS*, 213, 1
- Whittle, M. 1992(a), *ApJ*, 79, 49
- Whittle, M. 1992(b), *ApJ*, 387, 109
- Whittle, M. 1992(c), *ApJ*, 387, 121
- Wilson, A. S., Binette, L., & Storchi-Bergmann, T. 1997, *ApJ*, 482, L131
- Winter, L. M., Lewis, K. T., Koss, M., Veilleux, S., Keeney, B., & Mushotzky, R. F. 2010, *ApJ*, 710, 503
- Zakamska, N., et al. 2003, *AJ*, 126, 2125

TABLE 1
BLACK HOLE MASSES & OPTICAL NLR AND HOST GALAXY PROPERTIES OF TYPE-1 AGNs.

Galaxy	z	M_{BH}	$\log(L_{[\text{OIII}]})/(\text{ergs s}^{-1})$	$\sigma_{[\text{O III}]}(5007 \text{ \AA})$	σ_*
(-)	(-)	($10^7 M_{\odot}$)	(-)	(km s^{-1})	(km s^{-1})
(1)	(2)	(3)	(4)	(5)	(6)
2MASSJ09184900+2117170	0.1490	3.45 ± 0.35	42.09	274	...
2MASSJ1659397+183436	0.1709	174.28 ± 17.43	42.55	249	183 ± 10
2MASXJ10514428+3539304	0.1588	...	41.67	197	...
3C249.1	0.3110	187.10 ± 42.20	43.03	292	...
3C273	0.1583	88.60 ± 18.70	42.77	510	...
Ark120	0.0328	15.00 ± 1.90	41.34	209	...
CGCG121-075	0.0323	3.81 ± 0.38	41.56	238	...
ESO140-G043	0.0142	1.79 ± 0.18	41.09	89	...
FAIRALL9	0.0465	25.50 ± 5.60	42.08	181	...
IC4329A	0.0160	9.47 ± 0.95	41.28	234	122 ± 13
IRAS13342+3932	0.1793	66.61 ± 6.66	42.30	234	104 ± 14
IRAS13451+1232	0.1217	135.96 ± 13.60	42.22	511	157 ± 39
IRAS18216+6418	0.2970	120.00 ± 62.20	43.93	302	...
MCG-2-58-22	0.0469	83.13 ± 8.31	42.18	208	...
Mrk1014	0.1631	14.66 ± 3.01	42.96	324	200 ± 60
Mrk279	0.0305	3.49 ± 0.92	41.47	247	197 ± 12
Mrk335	0.0258	1.42 ± 0.37	41.52	119	...
Mrk493	0.0313	0.63 ± 0.06	40.66	393	...
Mrk590	0.0264	4.75 ± 0.74	41.24	182	192 ± 10
Mrk704	0.0295	13.64 ± 1.36	41.40	140	...
Mrk705	0.0290	39.63 ± 9.18	41.30	203	...
NGC3227	0.0039	2.43 ± 0.37	40.33	206	134 ± 6
NGC3516	0.0088	4.27 ± 1.46	40.91	106	235
NGC4051	0.0023	0.17 ± 0.05	39.66	81	87 ± 5
NGC4235	0.0080	...	39.53	170	143 ± 34
NGC5548	0.0172	8.20 ± 0.00	41.44	210	192 ± 15
NGC7469	0.0165	1.22 ± 0.14	41.54	153	142 ± 3
PG0026+129	0.1455	39.30 ± 9.60	42.46	191	...
PG0804+761	0.1010	69.30 ± 8.30	42.06	393	...
PG1119+120	0.0502	2.95 ± 0.59	41.49	249	162 ± 28
PG1229+204	0.0630	7.32 ± 3.52	41.68	197	162 ± 32
PG1351+640	0.0882	36.30 ± 7.26	42.19	390	...
PG1411+442	0.0896	44.30 ± 14.60	41.82	393	...
PG1426+015	0.0866	129.80 ± 38.50	41.89	287	217 ± 15
PG1440+356	0.0790	2.94 ± 0.59	41.48	393	...
PG1613+658	0.1295	27.90 ± 12.90	42.08	354	...
PG2130+099	0.0630	45.70 ± 5.50	41.93	296	172 ± 46
PG2349-014	0.1742	196.00 ± 19.60	43.11	221	223 ± 36
3C120*	0.0330	5.55 ± 2.70	41.62	122	162 ± 24
Mrk509*	0.0344	14.30 ± 1.20	42.33	221	...
NGC3783*	0.0097	2.98 ± 0.54	41.43	98	95 ± 10
NGC4151*	0.0033	4.57 ± 0.52	41.44	181	95 ± 7

NOTE.— (*) sources with MIR fine-structure lines resolved only by ISO.
Col. (3): When possible, M_{BH} measurements are taken from reverberation mapping experiments (Peterson et al. 2004; Bentz et al. 2006; Bentz et al. 2009; Denney et al. 2010). Otherwise, they are taken from single-epoch spectroscopy (Vestergaard & Peterson 2006; Kim et al. 2008) or computed from single-epoch spectroscopy (Marziani et al. 2003; Netzer & Traktenbrot 2007; Ho & Kim 2009; SDSS archival spectra) as in Vestergaard & Peterson (2006).
2MASXJ10514428+3539304 has weak, broad H_{α} detection but no H_{β} detection.
Col. (4): Data from Whittle (1992a), Marziani et al. (2003), Ho & Kim (2009), SDSS DR7, as well as our own measurements from the spectra presented in Boroson & Green (1992), performed as in Netzer & Traktenbrot (2007). The luminosities are not corrected for extinction.
Col.(5): $\sigma_{[\text{O III}]}$ values are taken from Whittle (1992a), Ho & Kim (2009), or measured from SDSS spectra.
Col. (6): Host galaxy velocity dispersion measurements are taken from Nelson et al. (2004), Onken et al. (2004), Dasyra et al. (2006a; 2006b; 2007), Ho (2007), and the 7th data release of SDSS. When more than one measurements were available, their average value was used. IRAS13451+1232 is a merger (Dasyra et al. 2006a). The velocity dispersion presented here corresponds to the combined value for both nuclei.

TABLE 2
BLACK HOLE MASSES & OPTICAL NLR AND HOST GALAXY PROPERTIES OF TYPE-2 AGNs.

Galaxy	z	M_{BH}	$\log(L_{[\text{OIII}]})/(\text{ergs s}^{-1})$	$\sigma_{[\text{O III}]}(5007 \text{ \AA})$	σ_*
(-)	(-)	($10^7 M_{\odot}$)	(-)	(km s^{-1})	(km s^{-1})
(1)	(2)	(3)	(4)	(5)	(6)
2MASXJ08035923+2345201	0.0297	...	40.99	121	130 ± 5
2MASXJ08244333+2959238	0.0254	...	41.13	157	107 ± 5
2MASXJ10181928+3722419	0.0497	...	41.33	155	100 ± 6
2MASXJ12384342+0927362	0.0829	...	41.97	233	229 ± 10
2MASXJ16164729+3716209	0.1518	...	42.51	150	229 ± 9
CGCG218-007	0.0273	...	40.85	131	149 ± 5
ESO103-G035	0.0133
IRAS05189-2524	0.0430	...	41.82	230	137 ± 16
IRAS15001+1433	0.1623	...	41.52	193	296 ± 19
IRAS18325-5926	0.0202
IRAS23060+0505	0.1730	...	42.24	243	...
MCG-03-34-064	0.0165
Mrk1066	0.0120	...	40.88	172	...
Mrk1457	0.0486	...	41.38	182	143 ± 6
Mrk273	0.0378	...	40.79	255	244 ± 18
Mrk3	0.0135	...	42.14	362	...
Mrk463E	0.0510	...	42.64	140	163 ± 8
Mrk609	0.0345	...	41.32	215	145 ± 4
Mrk622	0.0232	...	40.48	291	135 ± 5
NGC1068	0.0038	0.86 ± 0.03	41.80	451	151 ± 7
NGC1275	0.0174	...	41.68	601	246
NGC2622	0.0286	...	41.43	255	...
NGC2623	0.0185	...	39.01	140	152 ± 9
NGC2639*	0.0111	...	39.70	226	188
NGC3079*	0.0037	...	37.72	527	150
NGC4258	0.0018	3.78 ± 0.01	40.87	174	167
NGC4507	0.0118	...	41.53	91	...
NGC5256	0.0279	...	41.91	176	187 ± 8
NGC5506	0.0062	...	40.58	106	...
NGC5728	0.0094	...	41.12	136	...
NGC5929	0.0083	...	40.02	179	123 ± 3
NGC6240	0.0245	...	39.02	426	229 ± 43
NGC7172	0.0087
NGC7674	0.0290	...	42.01	189	...
SBS1133+572	0.0516	...	41.47	168	207 ± 7
UGC02608	0.0233
UGC5101	0.0394	...	39.91	193	188 ± 6
Centaurus A**	0.0018	4.90 ± 1.40	150 ± 7
Circinus**	0.0014	0.17 ± 0.03	38.55	...	80

NOTE.— (*) sources with shallow optical spectra, or spectra obtained under non photometric conditions.
(**) sources with MIR fine-structure lines resolved only by ISO.
Col. (3): M_{BH} measurements taken from Lodato & Bertin (2003), Greenhill et al. (2003), Herrnstein et al. (2005), and Neumayer et al. (2007). When more than one measurements were available, we used the value with the lower uncertainty.
Col.(4): The luminosities are computed from Whittle (1992a), Oliva et al. (1994), Veilleux et al. (1995; 1999), Ho et al. (1997a), Marziani et al. (2003) or measured from SDSS spectra. They are not corrected for extinction.
Col.(5): $\sigma_{[\text{O III}]}$ values taken from Heckman et al. (1983), Whittle (1992a), Veilleux et al. (1999), or measured from SDSS spectra.
Col. (6): Host galaxy velocity dispersions are compiled from Pahre (1999), Tecza et al. (2000), Tacconi et al. (2002), Dasyra et al. (2006b), Falcon-Barroso et al. (2006), Hinz & Rieke (2006), Müller Sánchez et al. (2006), Ho (2007), Cappellari et al. (2009), Gültekin et al. (2009), and from the 7th data release of SDSS.

TABLE 3
FLUXES AND VELOCITY DISPERSIONS OF IONIZED GAS NARROW LINES IN TYPE 1 AGNs.

Galaxy (-)	$f_{[\text{Ne II}]}$ (10^{-18} W m $^{-2}$)	$f_{[\text{S IV}]}$ (10^{-18} W m $^{-2}$)	$f_{[\text{Ne III}]}$ (10^{-18} W m $^{-2}$)	$f_{[\text{O IV}]}$ (10^{-18} W m $^{-2}$)	$f_{[\text{Ne V}]}$ (10^{-18} W m $^{-2}$)	$\sigma_{[\text{Ne II}]}$ (km s $^{-1}$)	$\sigma_{[\text{S IV}]}$ (km s $^{-1}$)	$\sigma_{[\text{Ne III}]}$ (km s $^{-1}$)	$\sigma_{[\text{O IV}]}$ (km s $^{-1}$)	$\sigma_{[\text{Ne V}]}$ (km s $^{-1}$)
2MASSJ09184900+2117170	< 3.61	< 10.86	15.65 \pm 2.39	...	< 25.07	206 \pm 35
2MASSJ1659397+183436	< 10.67	< 10.16	26.79 \pm 2.95	...	< 10.15	277 \pm 52
2MASXJ10514428+3539304	< 6.21	9.97 \pm 1.98	19.45 \pm 2.11	...	< 5.20	...	325 \pm 48
3C249.1	4.37 \pm 0.40	8.85 \pm 0.43	5.05 \pm 0.59	370 \pm 65	286 \pm 33	329 \pm 36
3C273	11.42 \pm 1.67	36.04 \pm 3.33	41.58 \pm 2.61	85.45 \pm 6.42	21.20 \pm 4.21	230 \pm 39	470 \pm 87	402 \pm 47	450 \pm 67	495 \pm 57
Ark120	28.97 \pm 2.53	< 13.56	35.23 \pm 2.71	36.84 \pm 3.70	10.04 \pm 1.61	202 \pm 32	...	213 \pm 38	190 \pm 39	...
CGCG121-075	24.88 \pm 1.44	24.39 \pm 2.00	47.28 \pm 1.96	85.25 \pm 1.86	16.36 \pm 1.25	...	209 \pm 50	238 \pm 42	220 \pm 27	223 \pm 43
ESO140-G043	96.32 \pm 2.92	87.41 \pm 2.95	139.5 \pm 2.2	247.6 \pm 4.9	79.10 \pm 2.19	203 \pm 29
FAIRALL9	21.50 \pm 1.85	28.59 \pm 3.86	44.80 \pm 3.44	63.73 \pm 3.68	20.79 \pm 3.77	...	296 \pm 45	197 \pm 36	258 \pm 48	231 \pm 42
IC4329A	241.5 \pm 6.2	245.7 \pm 9.5	535.0 \pm 6.8	1009 \pm 14	286.1 \pm 8.4	227 \pm 32	235 \pm 29	256 \pm 30	275 \pm 31	282 \pm 34
IRAS13342+3932	53.68 \pm 1.11	19.74 \pm 1.27	< 28.42	98.54 \pm 1.72	33.98 \pm 0.98	...	310 \pm 48	...	324 \pm 29	403 \pm 38
IRAS13451+1232	45.66 \pm 1.82	< 5.59	< 70.31	27.87 \pm 5.24	< 7.86	311 \pm 37	479 \pm 54	...
IRAS18216+6418	27.52 \pm 2.06	58.26 \pm 1.23	104.5 \pm 3.5	240.1 \pm 12.3	50.79 \pm 1.69	214 \pm 34	304 \pm 31	237 \pm 31	343 \pm 36	390 \pm 34
MCG-2-58-22	74.71 \pm 1.86	< 33.31	87.08 \pm 3.79	126.3 \pm 3.6	28.26 \pm 2.63	183 \pm 33	187 \pm 32	204 \pm 43
Mrk1014	58.26 \pm 1.42	33.20 \pm 1.67	93.20 \pm 2.96	119.9 \pm 5.8	46.01 \pm 2.39	253 \pm 37	376 \pm 36	379 \pm 41	379 \pm 39	380 \pm 48
Mrk279	81.42 \pm 2.88	26.48 \pm 2.04	80.35 \pm 3.97	102.8 \pm 3.6	34.80 \pm 2.19	215 \pm 34	237 \pm 36	222 \pm 35	...	248 \pm 42
Mrk335	10.54 \pm 0.90	< 25.80	22.56 \pm 1.75	130.0 \pm 3.7	12.88 \pm 1.86	155 \pm 17	247 \pm 64
Mrk493	62.69 \pm 1.31	< 23.47	27.09 \pm 1.53	28.42 \pm 4.76	9.59 \pm 1.27	280 \pm 39	267 \pm 46	280 \pm 38
Mrk590	32.81 \pm 2.12	< 16.58	21.14 \pm 2.54	31.04 \pm 3.06	9.57 \pm 1.64	197 \pm 33	200 \pm 33	206 \pm 40
Mrk704	< 10.05	< 61.44	< 50.82	< 151.67	51.08 \pm 3.04	249 \pm 37
Mrk705	52.30 \pm 1.90	< 23.26	49.59 \pm 2.11	57.82 \pm 2.19	30.18 \pm 1.66	192 \pm 31	210 \pm 35	280 \pm 39
NGC3227	708.7 \pm 25.2	220.9 \pm 5.5	725.8 \pm 6.2	668.0 \pm 17.6	231.2 \pm 7.5	...	241 \pm 32	228 \pm 30	216 \pm 29	209 \pm 34
NGC3516	74.01 \pm 2.29	128.9 \pm 4.4	164.4 \pm 2.9	458.4 \pm 5.5	67.57 \pm 2.18	198 \pm 30	229 \pm 28	...
NGC4051	172.6 \pm 4.9	< 47.59	162.0 \pm 2.9	347.6 \pm 7.1	107.7 \pm 3.9	172 \pm 29	295 \pm 27	...
NGC4235	34.85 \pm 1.62	< 6.03	33.29 \pm 1.77	33.60 \pm 3.04	< 5.28	214 \pm 34	286 \pm 43	...
NGC5548	83.08 \pm 3.32	42.90 \pm 2.55	81.76 \pm 2.77	124.7 \pm 8.6	31.50 \pm 2.16	177 \pm 30	...	206 \pm 38
NGC7469	1915 \pm 27	90.00 \pm 7.88	357.9 \pm 7.5	340.0 \pm 38.0	154.4 \pm 10.0	...	158 \pm 12	196 \pm 29	196 \pm 45	240 \pm 44
PG0026+129	2.56 \pm 0.33	4.94 \pm 0.43	< 7.72	20.16 \pm 4.01	< 5.07	305 \pm 40	...
PG0804+761	< 4.44	15.53 \pm 2.28	20.89 \pm 1.70	20.74 \pm 2.87	< 11.13	...	292 \pm 111	323 \pm 47	342 \pm 66	...
PG1119+120	< 4.00	20.63 \pm 2.55	28.41 \pm 2.01	60.00 \pm 2.37	16.16 \pm 2.33	193 \pm 47
PG1229+204	5.84 \pm 0.59	< 20.90	12.05 \pm 1.37	26.74 \pm 3.55	11.48 \pm 1.13	218 \pm 50
PG1351+640	21.92 \pm 0.99	< 10.26	29.39 \pm 1.73	< 12.38	< 3.83	200 \pm 43
PG1411+442	4.54 \pm 0.79	7.79 \pm 1.00	9.24 \pm 0.62	13.99 \pm 2.31	6.49 \pm 0.58	212 \pm 45	316 \pm 63
PG1426+015	13.46 \pm 1.08	13.67 \pm 2.28	25.55 \pm 1.09	29.51 \pm 4.38	8.47 \pm 1.09	226 \pm 38	...	258 \pm 36	292 \pm 57	289 \pm 57
PG1440+356	42.72 \pm 0.96	15.55 \pm 1.70	38.57 \pm 1.26	50.22 \pm 2.37	14.26 \pm 0.86	193 \pm 34	211 \pm 39	253 \pm 35	253 \pm 38	304 \pm 107
PG1613+658	37.66 \pm 1.23	13.25 \pm 1.01	30.90 \pm 1.02	66.49 \pm 3.15	< 7.92	226 \pm 30	269 \pm 33	289 \pm 33	225 \pm 29	...
PG2130+099	16.14 \pm 1.22	32.54 \pm 1.53	55.73 \pm 2.88	100.8 \pm 3.7	45.16 \pm 3.01	187 \pm 30	...	287 \pm 45
PG2349-014	15.95 \pm 0.71	< 6.36	20.51 \pm 1.01	34.73 \pm 3.82	< 6.83	273 \pm 48	...	259 \pm 34	308 \pm 35	...
3C120	78.86 \pm 3.72	225.7 \pm 3.3	271.6 \pm 3.7	1129 \pm 7	163.8 \pm 2.7	114 \pm 8	111 \pm 16
Mrk509	118.0 \pm 4.1	73.19 \pm 3.92	153.0 \pm 3.4	180.0 \pm 5.1	54.04 \pm 2.63	173 \pm 35	165 \pm 30	...
NGC3783	197.0 \pm 3.3	128.8 \pm 5.1	255.9 \pm 5.0	380.0 \pm 8.5	152.0 \pm 5.2	244 \pm 12	141 \pm 24	133 \pm 21
NGC4151	1180 \pm 12	1130 \pm 22	350.0 \pm 13.9	2030 \pm 33	560.0 \pm 11.0	...	207 \pm 16	155 \pm 7	169 \pm 12	139 \pm 25

NOTE.—No data for the line fluxes indicate no spectral coverage at the observed-frame wavelengths of these lines. No data for the velocity dispersion of detected lines indicate that their signal to noise ratio was between 3 and 5, or that their profiles were unresolved.

TABLE 4
FLUXES AND VELOCITY DISPERSIONS OF IONIZED GAS NARROW LINES IN TYPE 2 AGNs.

Galaxy (-)	$f_{[\text{Ne II}]}$ (10^{-18} W m $^{-2}$)	$f_{[\text{S IV}]}$ (10^{-18} W m $^{-2}$)	$f_{[\text{Ne III}]}$ (10^{-18} W m $^{-2}$)	$f_{[\text{O IV}]}$ (10^{-18} W m $^{-2}$)	$f_{[\text{Ne V}]}$ (10^{-18} W m $^{-2}$)	$\sigma_{[\text{Ne II}]}$ (km s $^{-1}$)	$\sigma_{[\text{S IV}]}$ (km s $^{-1}$)	$\sigma_{[\text{Ne III}]}$ (km s $^{-1}$)	$\sigma_{[\text{O IV}]}$ (km s $^{-1}$)	$\sigma_{[\text{Ne V}]}$ (km s $^{-1}$)
2MASXJ08035923+2345201	< 6.39	< 5.50	18.78 \pm 2.08	28.45 \pm 1.59	< 4.75	203 \pm 42
2MASXJ08244333+2959238	33.17 \pm 2.04	< 20.88	49.47 \pm 3.44	83.64 \pm 2.13	36.14 \pm 2.78	207 \pm 39	264 \pm 30
2MASXJ10181928+3722419	8.67 \pm 1.53	< 6.35	14.69 \pm 1.87	28.81 \pm 1.60	16.59 \pm 2.80	200 \pm 32
2MASXJ12384342+0927362	< 8.33	20.09 \pm 2.25	27.85 \pm 2.15	58.83 \pm 2.38	12.94 \pm 2.35	...	232 \pm 42	260 \pm 42	261 \pm 36	265 \pm 73
2MASXJ16164729+3716209	< 5.34	16.53 \pm 1.49	22.55 \pm 2.52	90.14 \pm 2.28	17.88 \pm 2.23	211 \pm 37
CGCG218-007	102.6 \pm 3.1	35.72 \pm 2.64	86.07 \pm 2.69	166.7 \pm 2.3	46.59 \pm 1.98	215 \pm 33
ESO103-G035	294.0 \pm 7.6	115.1 \pm 10.1	414.0 \pm 9.4	311.7 \pm 13.9	172.9 \pm 10.5	223 \pm 37	232 \pm 34	276 \pm 31	240 \pm 35	346 \pm 52
IRAS05189-2524	191.8 \pm 8.9	65.30 \pm 6.26	186.1 \pm 7.1	261.2 \pm 37.2	152.6 \pm 12.0	253 \pm 42	335 \pm 55	392 \pm 41	444 \pm 63	404 \pm 43
IRAS15001+1433	66.48 \pm 1.36	4.74 \pm 0.82	27.97 \pm 0.69	21.78 \pm 3.21	15.89 \pm 1.97	247 \pm 34	388 \pm 36	348 \pm 38	558 \pm 96	422 \pm 81
IRAS18325-5926	367.9 \pm 7.8	114.9 \pm 8.2	436.0 \pm 5.3	390.7 \pm 12.2	262.6 \pm 9.6	181 \pm 31	265 \pm 39	367 \pm 32	300 \pm 34	404 \pm 64
IRAS23060+0505	32.26 \pm 2.40	19.65 \pm 2.34	25.61 \pm 2.10	35.31 \pm 5.45	20.12 \pm 2.69	278 \pm 59	366 \pm 127	285 \pm 62	343 \pm 57	419 \pm 62
MCG-03-34-064	514.9 \pm 8.2	476.1 \pm 8.3	1150 \pm 13	1053 \pm 22	615.6 \pm 8.2	344 \pm 34	298 \pm 33	361 \pm 28	273 \pm 30	435 \pm 36
Mrk1066	1094 \pm 21	102.0 \pm 7.4	469.1 \pm 7.6	418.1 \pm 22.1	92.38 \pm 8.31	216 \pm 32	284 \pm 41	246 \pm 48
Mrk1457	91.99 \pm 2.39	< 14.09	38.13 \pm 4.09	28.10 \pm 2.54	22.09 \pm 3.04	228 \pm 43	310 \pm 60
Mrk273	444.9 \pm 7.9	101.7 \pm 2.3	338.1 \pm 2.5	550.1 \pm 17.8	112.3 \pm 3.7	252 \pm 30	357 \pm 34	332 \pm 30	357 \pm 38	406 \pm 32
Mrk3	979.8 \pm 10.2	592.7 \pm 6.2	1749 \pm 11	1964 \pm 24	632.5 \pm 7.5	276 \pm 29	322 \pm 29	314 \pm 29	263 \pm 28	327 \pm 31
Mrk463E	108.2 \pm 3.5	275.0 \pm 5.4	404.6 \pm 7.3	641.8 \pm 11.3	193.9 \pm 4.7	308 \pm 35	284 \pm 30	235 \pm 29	295 \pm 29	287 \pm 31
Mrk609	213.5 \pm 6.2	< 22.18	56.71 \pm 2.53	82.43 \pm 25.69	38.69 \pm 4.28	202 \pm 36	...	488 \pm 60
Mrk622	97.29 \pm 13.80	< 8.61	49.29 \pm 2.82	< 37.42	< 38.06	333 \pm 34
NGC1068	4988 \pm 183	6199 \pm 336	13781 \pm 246	20406 \pm 473	8974 \pm 221	359 \pm 52	414 \pm 44	383 \pm 31	364 \pm 48	363 \pm 39
NGC1275	461.5 \pm 8.0	< 16.26	223.7 \pm 5.6	< 84.37	< 11.65	299 \pm 31	...	260 \pm 31
NGC2622	62.02 \pm 2.63	< 18.46	80.41 \pm 2.93	89.29 \pm 3.58	24.73 \pm 2.08	213 \pm 33	...	289 \pm 39
NGC2623	550.1 \pm 9.7	11.20 \pm 1.36	147.2 \pm 1.7	117.4 \pm 18.2	37.55 \pm 2.97	213 \pm 31	357 \pm 52	222 \pm 39
NGC2639	86.23 \pm 2.66	< 6.90	48.88 \pm 1.95	< 23.82	< 7.51	346 \pm 43	...	336 \pm 49
NGC3079	1310 \pm 60	< 14.61	238.3 \pm 3.3	< 94.19	< 38.79	198 \pm 33	...	285 \pm 29
NGC4258	123.5 \pm 7.3	< 15.61	70.61 \pm 5.61	79.40 \pm 8.03	< 13.67	193 \pm 42	...	191 \pm 36	204 \pm 53	...
NGC4507	307.8 \pm 6.9	93.08 \pm 6.84	287.8 \pm 6.3	354.1 \pm 11.6	125.7 \pm 6.4	220 \pm 35	318 \pm 42	345 \pm 81
NGC5256	160.6 \pm 3.1	27.06 \pm 1.56	94.40 \pm 1.45	569.8 \pm 10.3	20.54 \pm 1.37	227 \pm 29	239 \pm 37	227 \pm 30	191 \pm 28	202 \pm 40
NGC5506	850.6 \pm 14.3	735.4 \pm 15.6	1537 \pm 11	2262 \pm 40	568.0 \pm 10.6	...	239 \pm 33	207 \pm 28	...	208 \pm 32
NGC5728	366.2 \pm 7.7	317.2 \pm 8.2	536.5 \pm 6.7	1155 \pm 12	217.1 \pm 3.4	...	272 \pm 41	263 \pm 29	306 \pm 30	314 \pm 32
NGC5929	104.8 \pm 2.2	12.41 \pm 1.98	95.07 \pm 1.40	43.67 \pm 6.18	< 6.09	210 \pm 28
NGC6240	1872 \pm 29	38.7 \pm 2.9	599.9 \pm 4.2	374.0 \pm 35.9	90.24 \pm 9.02	362 \pm 37	279 \pm 52	341 \pm 29
NGC7172	334.6 \pm 8.1	55.74 \pm 4.43	168.1 \pm 4.0	384.4 \pm 5.3	90.23 \pm 3.49	256 \pm 30	...	204 \pm 30
NGC7674	215.7 \pm 5.2	152.6 \pm 5.9	346.0 \pm 6.5	442.9 \pm 12.1	184.4 \pm 7.0	...	267 \pm 34	253 \pm 32	242 \pm 32	267 \pm 39
SBS1133+572	108.3 \pm 2.9	42.01 \pm 3.62	105.3 \pm 3.8	168.7 \pm 2.8	69.89 \pm 2.87	...	248 \pm 40
UGC02608	566.5 \pm 9.4	292.8 \pm 9.5	706.3 \pm 6.1	1378 \pm 17	312.9 \pm 5.1	...	213 \pm 31
UGC5101	379.7 \pm 9.0	< 7.34	146.2 \pm 2.1	57.18 \pm 9.66	34.19 \pm 3.73	254 \pm 40	...	350 \pm 34	285 \pm 41	385 \pm 40
Centaurus A	2210 \pm 45	140.0 \pm 9.6	1400 \pm 12	980.0 \pm 42.2	200.0 \pm 8.5	220 \pm 31	...	134 \pm 21	127 \pm 9	132 \pm 21
Circinus	4536 \pm 145	1270 \pm 58	4000 \pm 90	6793 \pm 420	2180 \pm 101	...	91 \pm 6	86 \pm 4	113 \pm 3	90 \pm 8

NOTE.—Same as in Table 3

TABLE 5
ESTIMATES OF M_{BH} IN TYPE-2 AGN.

Galaxy (-)	$M_{\text{BH}}(\sigma_{*}^{4.24})$ ($10^7 M_{\odot}$)	$M_{\text{BH}}(\sigma_{\text{NLR}}^{4.24})$ ($10^7 M_{\odot}$)	M_{BH} (plane equation) ($10^7 M_{\odot}$)
2MASXJ08035923+2345201	2.1	9.3	4.4
2MASXJ08244333+2959238	0.9	17	7.5
2MASXJ10181928+3722419	0.7	5.3	7.3
2MASXJ12384342+0927362	23	19	16
2MASXJ16164729+3716209	23	6.6	22
CXCG218-007	3.8	7.2	7.3
ESO103-G035	...	29	8.4
IRAS05189-2524	2.7	132	29
IRAS15001+1433	70	225	41
IRAS18325-5926	...	70	17
IRAS23060+0505	...	75	45
MCG-03-34-064	...	76	22
Mrk1066	...	20	7.9
Mrk1457	3.2	24	10
Mrk273	31	82	28
Mrk3	...	40	19
Mrk463E	5.5	26	36
Mrk609	3.4	120	14
Mrk622	2.5	76	9.0
NGC1275	32	27	11
NGC2622	...	18	8.2
NGC2623	4.1	37	7.5
NGC2639	10	80	4.7
NGC3079	3.9	40	3.0
NGC4507	...	41	8.4
NGC5256	9.9	9.2	8.1
NGC5506	...	8.8	6.0
NGC5728	...	32	8.7
NGC5929	1.7	11	3.0
NGC6240	23	51	17
NGC7172	...	9.5	4.0
NGC7674	...	19	16
SBS1133+572	15	12	11
UGC02608	...	6.0	11
UGC5101	10	71	17

NOTE.— The second column corresponds to the result of the stellar $M_{\text{BH}} - \sigma$ relation. The third column presents the M_{BH} estimate using the $M_{\text{BH}} - \sigma$ relation for the NLR, as found in Figure 10. The fourth column uses the plane equation presented in Figure 12. For the NLR gas-based estimates, we present the average value using all resolved lines. Formal, statistical M_{BH} uncertainties are of a factor of 0.5 dex. For individual sources the uncertainty can be higher, typically within an order of magnitude.